

# The Radio Scream at Cosmic Dawn: A Semi-Analytic Model for the Impact of Radio Loud Black-Holes on the 21 cm Global Signal

Aaron Ewall-Wice,<sup>1\*</sup> Tzu-Ching Chang<sup>1,2</sup>, T. Joseph W. Lazio<sup>1</sup>

<sup>1</sup>*Jet Propulsion Laboratory, California Institute of Technology 4800 Oak Grove Dr, M/S 169-237, Pasadena CA 91109, USA*

<sup>2</sup>*California Institute of Technology, 1200 E California Blvd, Pasadena, CA 91125, USA*

Accepted XXX. Received YYY; in original form ZZZ

## ABSTRACT

We use a semi-analytic model to explore the impact of radio-loud black-holes on the H I hyperfine 21 cm signal during the Cosmic Dawn. Our formalism for black-hole growth can be incorporated into existing 21 cm simulations. We find that radio emission from super-massive black hole seeds can impact the global 21 cm signal at the level of tens to hundreds of percent provided that they were radio loud and obscured by gas with column depths of  $N_{\text{H}} \gtrsim 10^{23} \text{ cm}^{-2}$ . We find various sets of parameters that reproduce some of the striking features of the EDGES absorption feature including its depth, timing, and side steepness while producing radio/X-ray backgrounds and source counts that are consistent with published limits. Scenarios yielding a dramatic 21 cm signature also predict large populations of  $\sim \mu\text{Jy}$  point sources that will be detectable in upcoming deep surveys from the Square Kilometer Array (SKA). Thus, 21 cm measurements, complemented by deep point source surveys, have the potential to constrain the radio properties of super-massive black-hole progenitors.

**Key words:** keyword1 – keyword2 – keyword3

## 1 INTRODUCTION

Before stars and quasars established strong ionizing backgrounds, most of the Hydrogen in the Universe existed as H I in the intergalactic medium (IGM). Since H I’s hyperfine transition is sensitive to astrophysical backgrounds, its emitted 21 cm photons carry considerable information on the first sources of radiation such as stars, supernovae, black holes, and dark matter. (For reviews, see [Furlanetto et al. 2006](#); [Morales & Wyithe 2010](#); [Pritchard & Loeb 2012](#); [McQuinn 2016](#)))

A long-standing question that 21 cm observations might help resolve is how  $\gtrsim 10^9 M_{\odot}$  super-massive black holes (SMBH) observed at  $z \sim 7$  ([Mortlock et al. 2011](#); [Wu et al. 2015](#); [Bañados et al. 2018](#)) could assemble from much smaller seeds in less than a billion years. Several studies have investigated how 21 cm observations might reveal the heating and ionization of H I in the intergalactic medium (IGM) due to the X-ray or ultraviolet (UV) emission from accreting black-hole seeds ([Madau et al. 2004](#); [Zaroubi et al. 2007](#); [Ripamonti et al. 2008](#); [Madau & Haardt 2015](#); [Tanaka et al. 2016](#)). Ra-

dio emission, a well-known product of accretion on to black holes, has received almost no consideration.

This lack of attention is reasonable. It has long been recognized that the diffuse lobes, that dominate radio emission in many low-redshift active galactic nuclei (AGN), should be suppressed at high redshift. The higher energy density of the Cosmic Microwave Background (CMB) is expected to cause relativistic electrons to shed their energy through inverse Compton (IC) scattering instead of synchrotron emission (e.g., [Ghisellini et al. 2014, 2015](#); [Saxena et al. 2017](#)). IC suppression of synchrotron emission may partially explain the dearth of SDSS quasars matched with radio sources at  $z \gtrsim 3$  ([Haiman et al. 2004](#); [McGreer et al. 2009](#); [Volonteri et al. 2011](#)). In addition, some studies (e.g., [Jiang et al. 2007](#)) claim tentative detections of decreasing radio loud source densities at high redshift.<sup>1</sup>

At the same time, observations of the highest redshift radio sources by [Bañados et al. \(2015\)](#) find no evidence for a decrease in the radio-loud fraction while [Ghisellini & Sbarato \(2016\)](#) find that the lack of radio-loud SDSS quasars

<sup>1</sup> While its specific definition varies throughout the literature, we define “radio-loudness” as the  $\log_{10}$ -ratio between 2.8 GHz luminosity and 8000 Å luminosity observed at the redshift of emission.

\* E-mail: aaron.m.ewall-wice@jpl.nasa.gov

relative to known blazar counts might be heavily influenced by obscuration. It is entirely possible that the first black-hole seeds had high spins, large magnetic fields, and accreted in dense environments that could allow the relativistic electrons in their jets to have emitted the bulk of their energy through radio synchrotron emission, despite the higher CMB energy densities. The nature and evolution of radio emission from the highest redshift black-holes remain essentially unconstrained by direct measurements.

The question as to whether black-holes between  $10 \lesssim z \lesssim 30$  generated appreciable radio emission is made more compelling by tentative observations by the ARCADE-2 (Fixsen et al. 2011) and EDGES (Bowman et al. 2018) (B18) experiments. The first, made at  $\sim$  GHz frequencies, observes a radio monopole that exceeds the level expected from known populations of extragalactic radio sources. Recent observations by the Long Wavelength Array between 40 and 80 MHz lend further support for the existence of such a background (Dowell & Taylor 2018), though it is still unclear whether it arises from lower redshifts or is purely a result of observational systematics (Singal et al. 2018). The EDGES feature, at  $\sim$  70 MHz reports a 21 cm absorption trough with an amplitude that greatly exceeds what is possible for adiabatically cooled HI gas absorbing solely the CMB background.

One possible explanation for the unusual timing and depth of the EDGES feature might be an enhanced radio background, similar to what was reported by ARCADE-2 and originating at  $z \gtrsim 17$  (Feng & Holder 2018; Fialkov & Barkana 2019). If confirmed, this radio background might be sourced by black-holes (Ewall-Wice et al. 2018), star forming galaxies (SFGs) (Mirocha & Furlanetto 2018), annihilations of an axion-like dark-matter particle (Fraser et al. 2018) or dark photons (Pospelov et al. 2018).

If early accreting black-holes were radio-loud, their emission might have an observable effect on the 21 cm signal. Should this be the case, a self-consistent model for black-hole radio emission, along with other mechanisms for radio emission (such as star-forming galaxies, axions, or dark photons) will be necessary to interpret 21 cm observations. Such models will also be needed to distinguish a radio-background explanation for EDGES from alternative theories such as dark matter cooling (Barkana 2018; Barkana et al. 2018; Muñoz & Loeb 2018; Fialkov et al. 2018; Berlin et al. 2018) or systematics (Hills et al. 2018). Radio background models can also be used to predict discrete radio source populations that might be detected in surveys.

In a previous paper, Ewall-Wice et al. (2018), we estimated the amplitude of the radio background that might arise from vigorously accreting black-hole seeds at high redshift and discussed the potential for such a radio background to explain EDGES assuming saturated Ly- $\alpha$  coupling of the spin-temperature,  $T_s$ , to the gas kinetic temperature,  $T_k$ . We ignored X-ray heating from the same sources. Our conclusions in this paper were overly generous since heating and incomplete Ly  $\alpha$  coupling can both reduce the amplitude of the Cosmic Dawn absorption signal. The logical next step in any modeling effort is to self-consistently compute the 21 cm signal under the influence of all radiative outputs from accreting black holes and star formation; including the effects of radio, X-ray heating, Ly  $\alpha$  coupling, and UV/X-ray ionization.

In this follow-up study, we construct a semi-analytic model to predict the evolution of the global 21 cm signal under the influence of accreting black-holes radiating across the electromagnetic spectrum; from radio waves to X-rays. We use this model to determine how radio emission from the first black-holes might appear in global 21 cm observations. We also explore whether these radio-loud black-holes might explain the EDGES feature and what scenarios might be detected in current and up-coming radio surveys.

This paper is organized as follows. We begin with an overview of the existing global-signal framework in § 2 before describing the modifications introduced by black-hole seeds in § 3. We explore the impact of radio-loud accretion on the global signal in § 4 by computing the global-signal for a variety of illustrative models. We explore the degeneracies in several models that yield an absorption feature similar to the one reported by EDGES in § 5, how they might be broken by upcoming point-source surveys, and discuss which features we are and are not able to reproduce. We conclude in § 6.

## 2 THE MODELING FRAMEWORK

Luminous sources affect the physical properties of HI in the IGM by setting up radiative backgrounds. Throughout this paper, we assume that the co-moving emissivity of radiation, with frequency  $\nu$ , at position  $\mathbf{x}$  and redshift  $z$  is the sum of contributions from stars/stellar remnants and AGN, which we denote as  $\epsilon_\star$  and  $\epsilon_\bullet$  respectively.

$$\epsilon(\mathbf{x}, z, \nu) = \epsilon_\star(\mathbf{x}, z, \nu) + \epsilon_\bullet(\mathbf{x}, z, \nu). \quad (1)$$

In this section, we describe the existing framework for computing the global 21 cm signal and previously derived expressions for  $\epsilon_\star$ . In the next section we will discuss how we modify this framework by adding accreting radio-loud black-holes. We will start out with a review of the existing frameworks for computing  $\epsilon_\star$  for Ly  $\alpha$  (§ 2.1), X-ray (§ 2.2), and UV continuum (§ 2.3) photons. We end this section with a description of how radiative backgrounds impact the observable 21 cm brightness temperature,  $\delta T_b$  (§ 2.4).

In this work, we choose to ignore radio emission from X-ray binaries since, in the local Universe, they are roughly four orders of magnitude less radio loud than AGN (Heinz & Sunyaev 2003) and their total contribution to the radio background is negligible compared to star-forming galaxies and AGN. In addition, should such sources exist in large enough abundance to produce a large radio background, obscuring them would likely be more difficult than a central AGN. A study by Das et al. (2017) finds that most XRBs in the early universe would have column depths too small to prevent  $\approx$  1 keV X-rays from significantly heating intergalactic gas.

### 2.1 Ly $\alpha$ Emission

Ly  $\alpha$  photons primarily impact the 21 cm signal by coupling the HI spin temperature,  $T_s$ , to its kinetic temperature  $T_k$  through a multiplicative coupling constant,  $x_\alpha$  (see equation 7 below).

As outlined in Hirata (2006), whose recipe we employ here,  $x_\alpha$  as proportional to the Ly  $\alpha$  number flux,  $J_\alpha$ .  $J_\alpha$

includes a contributions from secondary photons stimulated by X-rays, ( $J_{\alpha,X}$ ) and a contribution from atoms excited by UV continuum photons that redshift into the Ly  $n \geq 2$  transitions ( $J_{\alpha,UV}$ ). We compute  $J_{\alpha,UV}$  using the prescription in Hirata (2006).

$$J_{\alpha,UV}(z) = \sum_{n=2} f_{\text{rec}}(n) \frac{c(1+z)^2}{4\pi} \int_z^{z_{\text{max}}(n)} \frac{\epsilon_{UV}[\nu_n(z, z'), z']}{H(z') h_P \nu_n(z, z')} dz', \quad (2)$$

where  $h_P$  is Planck's constant,  $\nu_n(z, z')$  is the emitted frequency of a photon at  $z'$  that redshifts into the Ly  $n$  resonance at redshift  $z$ ,  $f_{\text{rec}}(n)$  is the probability of an absorbed Ly  $n$  photon being re-emitted as a Ly  $\alpha$  photon, and  $z_{\text{max}}(z, n)$  is the maximum redshift from which a Ly  $n$  photon can be emitted without redshifting into Ly  $(n-1)$  and being absorbed before reaching redshift  $z$ .

We write the co-moving emissivity of UV photons with frequency  $\nu$  from redshift  $z$  as  $\epsilon_{UV}(\nu, z)$ . We split  $\epsilon_{UV}$  into contributions from stars,  $\epsilon_{UV\star}$ , and black holes,  $\epsilon_{UV\bullet}$ . Here we focus on the stellar contribution and will discuss the black-hole contribution in § 3.2.2. We set  $\epsilon_{UV\star}$  to be proportional to the star formation rate density.

$$\epsilon_{UV\star}(\nu, z) = h_P \nu f_{\star} N_{\gamma} n_{UV}(\nu) \frac{\Omega_b}{\Omega_m} \frac{\dot{\rho}_{\text{coll}\star}(z)}{\mu m_p}, \quad (3)$$

where  $f_{\star}$  is the fraction of baryons incorporated into stars,  $\mu$  is the reduced particle mass of the IGM,  $m_p$  is the proton mass,  $N_{\gamma}$  is the average number of ionizing photons emitted per stellar baryon, and  $n_{UV}(\nu)$  is the differential number of photons emitted per unit frequency divided by  $N_{\gamma}$  calculated in Barkana & Loeb (2005). The quantity  $\rho_{\text{coll}\star}$  is the *total* comoving density of matter collapsed in halos with virial-temperatures above a minimum threshold,  $T_{\text{vir}\star}^{\text{min}}$  computed from the Sheth & Tormen (1999) mass function. The values for  $f_{\star}$  and  $N_{\gamma}$  are currently unknown. As fiducial values, we adopt  $f_{\star} = 0.1$  and  $N_{\gamma} = 2000$ , which yields an ionization history that is consistent with the joint constraints derived from measurements of the CMB optical depth, quasar absorption features, and the kinetic Sunyaev Zeldovich effect (Greig & Mesinger 2017).

## 2.2 X-rays

X-rays from early galaxies are thought to have had a significant impact on the physical state of H I during the Cosmic Dawn, primarily by heating the gas (raising  $T_k$ ) but also by ionizing it (raising the electron fraction,  $x_e$ ) and stimulating secondary UV photons. At low redshifts, X-ray emission from star-forming galaxies is contributed to by two types of sources. First are high-mass X-ray binaries and hot ISM generated by supernovae (Pacucci et al. 2014) whose emissivities are proportional to star formation rate. Secondly, low-mass X-ray binaries contribute emission that traces the total star formation history. At higher redshifts, high mass X-ray binaries and ISM dominate. We therefore adopt an X-ray emissivity based on the empirical X-ray luminosity star formation rate density relation that appears in much of the 21 cm literature (e.g. Oh (2001), Mirabel et al. (2011), Filalkov et al. (2014), Mesinger et al. (2013)).

$$\begin{aligned} \epsilon_{X\star}(E) = & 3 \times 10^{39} \text{ erg sec}^{-1} \text{ keV}^{-1} f_X \left( h^2 M_{\odot} \text{ yr}^{-1} \text{ Mpc}^{-3} \right)^{-1} \frac{\Omega_b}{\Omega_m} \\ & \times A_{2,10}(\alpha_{X\star}) f_{\star} \dot{\rho}_{\text{coll}\star}(z) \left( \frac{E}{\text{keV}} \right)^{-\alpha_{X\star}} \\ & \times \exp \{ -N_{H\star} [\sigma_H(E) + \chi \sigma_{\text{HeI}}(E)] \}, \end{aligned} \quad (4)$$

where  $N_{H\star}$  is the Hydrogen column density to the X-ray sources,  $\sigma_H(E)$  and  $\sigma_{\text{HeI}}(E)$  are the Hydrogen and Helium photo-ionization cross sections,  $\chi$  is the ratio between Helium and Hydrogen number densities<sup>2</sup>, and  $A_{2,10}(\alpha_X) \equiv (1 - \alpha_X)(10^{1-\alpha_X} - 2^{1-\alpha_X})^{-1}$  is a normalization factor ensuring that when  $f_X = 1$ , the 2-10 keV emissivity matches observations of local star-forming galaxies by Mineo et al. (2012). We compute X-ray ionization, heating, and the generation of secondary Ly  $\alpha$  photons using standard radiative transfer recipes using interpolation of the numerical cross sections from Furlanetto & Stoever (2010)<sup>3</sup>. To compute  $I_X$  at redshift  $z$ , we integrate the contributions of sources at higher redshifts and evolve the kinetic temperature and X-ray ionization fractions using equations 8 and 9 in Mesinger et al. (2011) (M11). We adopt fiducial values of  $f_X = 1$ ,  $\alpha_{X\star} = 1.2$ , and  $N_{H\star} = 10^{21}$  which are typical values obtained in numerical simulations of early galaxies (Das et al. 2017).

## 2.3 Ionizing UV Continuum Photons

The majority of Hydrogen reionization was probably driven by UV photons generated by star formation and/or AGN activity. We track the evolution of the volumetric fraction of H II regions  $x_i$  through the differential equation,

$$\dot{x}_i = \frac{4}{4 - 3Y_p} f_{\text{esc}\star} f_{\star} N_{\gamma} \frac{\dot{\rho}_{\text{coll}\star}(z)}{\rho_0} - n_{H,0} x_i C(z) \alpha_A(T_4) (1+z)^3, \quad (5)$$

where  $f_{\text{esc}\star}$  is the escape-fraction for stellar UV photons;  $n_{H,0}$  is the comoving number density of Hydrogen atoms;  $\alpha_A$  is the case A recombination coefficient;  $T_4$  is the electron temperature in H II regions, which we take to be  $10^4$  K; and  $C(z)$  is the clumping factor, which we set equal to  $C(z) = 2.9 \times ((1+z)/6)^{-1.1}$  (Madau & Haardt 2015). We choose  $f_{\text{esc}\star} = 0.1$  as a fiducial value. We note that the  $x_i$  in equation 5 refers to H II regions generated by UV photons. Ionizations from X-rays are handled separately by evolving  $x_e$  using equations 8 and 9 in M11.

## 2.4 The 21 cm Brightness Temperature

The 21 cm brightness temperature  $\delta T_b(\mathbf{x})$  is a function of position while the ‘‘global’’ signal is equal to the ensemble average,  $\langle \delta T_b(\mathbf{x}) \rangle$ . As we will only be discussing the average

<sup>2</sup>  $\chi = Y_P / 4 / (1 - Y_P)$  where  $Y_P$  is the cosmological Helium mass fraction.

<sup>3</sup> for example, see M11

“global” 21 cm signal, we let  $\delta T_b \equiv \langle \delta T_b(\mathbf{x}) \rangle$ . We approximate  $\delta T_b$  using the equation<sup>4</sup>

$$\delta T_b \approx 27 x_{\text{HI}} \left( \frac{\Omega_b h^2}{0.023} \right) \left( \frac{0.15}{\Omega_m h^2} \right) \left( 1 - \frac{T_r}{T_s} \right) \sqrt{\frac{1+z}{10}} \text{ mK} \quad (6)$$

where  $T_r$  is the average brightness temperature of the 21 cm radio background at redshift  $z$ ,  $T_s$  is the H I spin-temperature,  $x_{\text{HI}}$  is the average neutral fraction,  $\Omega_b$  and  $\Omega_m$  are the fractions of the critical energy density in baryons and matter respectively, and  $h = H_0/100 \text{ km sec}^{-1} \text{ Mpc}^{-1}$  where  $H_0$  is the Hubble constant.  $T_r$  is typically set to be equal to the temperature of the CMB,  $T_r = T_{\text{CMB}}$ . In this paper, we consider an additional contribution to  $T_r$  from AGN. The coupling of H I’s spin temperature  $T_s$ , to its kinetic temperature  $T_k$ ,  $T_r$ , and the Ly  $\alpha$  color temperature  $T_\alpha$ , is described by (Field 1958)

$$T_s^{-1} = \frac{T_r^{-1} + x_\alpha T_\alpha^{-1} + x_c T_k^{-1}}{1 + x_\alpha + x_c}, \quad (7)$$

where  $x_\alpha$  and  $x_c$  are the Ly  $\alpha$  and collisional coupling constants. The factor  $x_\alpha$  is determined by the Ly  $\alpha$  flux relative to the radiative background while  $x_c$  is determined by the density, temperature, and ionization state of H I (Furlanetto et al. 2006). In this work, the radio temperature,  $T_r$  arises from the CMB and the radio background from black-holes.

$$T_r(\nu, z) = T_{\text{CMB}}(z) + \frac{\lambda_{21}^2}{2k_B} \frac{c(1+z)^3}{4\pi} \int \epsilon_{\text{R}\bullet} \left[ \nu \frac{1+z'}{1+z}, z' \right] (1+z')^{-1} H^{-1}(z') dz', \quad (8)$$

where  $\epsilon_{\text{R}\bullet}(\nu, z)$  is the co-moving radio emissivity of black-holes at frequency  $\nu$  and redshift  $z$  which we discuss in detail in § 4.4,  $k_B$  is the Boltzmann constant,  $c$  is the speed of light in vacuum, and  $H(z)$  is the Hubble parameter at redshift  $z$ . The Lyman- $\alpha$  color temperature is computed from  $T_\alpha(z) = \frac{\lambda_\alpha^2}{2k_B} I_\alpha(z)$  where  $I_\alpha(z)$  is the background intensity of Lyman- $\alpha$  photons from the de-excitation of Ly  $n$  states and secondary production by X-rays (§ 2.1).

In addition to the heating from X-rays (§ 2.2), we also include the impacts of adiabatic cooling, Compton heating, and ionization induced changes in thermal degrees of freedom when evolving  $T_k$ .

While X-rays are expected to be the primary drivers of IGM heating, recent work by Venumadhav et al. (2018) (V18) finds that a radio-background can have a significant impact on  $T_k$  when the IGM is unheated. We include X-rays in this work and also find that some heating has occurred at the absorption minimum in all of our models. We therefore choose to ignore the V18 CMB heating mechanism in this paper.

<sup>4</sup> For our computation of the global signal, the terms in equation 6 are their volume averaged quantities which ignores the spatial correlations that exist between  $x_{\text{HI}}$ ,  $T_s$ ,  $T_r$ , and the density field. Liu et al. (2016) find that this approximation has a  $\sim 10\%$  impact on the global signal amplitude though their analysis ignored  $T_s$ .

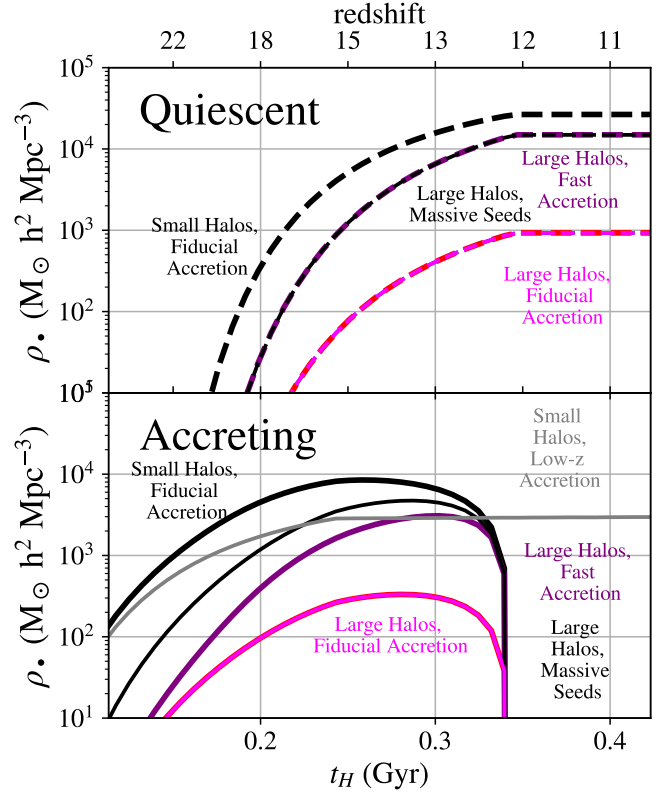


**Figure 1.** The evolution of the quiescent black-hole density  $\rho_{\bullet q}$  (top panel) and the accreting black-hole density  $\rho_{\bullet a}$  (bottom panel). Seed formation cuts off at  $z_{\text{min}}^i = 16$  for all of our models, causing  $\rho_{\bullet a}$  to level off. With an accretion lifetime of 100 Myr,  $\rho_{\bullet a}$  drops to zero 100 Myr later at  $z \approx 12$ . Lower halo mass thresholds and/or higher mass seeds translate the onset of density growth to earlier times while smaller black-hole mass e-folding (Salpeter) times increase its steepness. Note that in our model, the number density, not overall mass, of halos determines the black-hole density. Thus Large Halos scenarios have fewer black holes (and overall lower average black hole density) than the Small Halos model.

### 3 MODELING THE BLACK-HOLES

We now discuss how we add the impact of radiation from exponentially growing black-hole seeds to the global signal framework described in § 2. We start with a simple equation that allows us to compute the black-hole density as a function of redshift (§ 3.1). Assuming that our black-holes grow and radiate through Eddington limited accretion allows us to compute their comoving emissivity across the electromagnetic spectrum § 3.2.

#### 3.1 Evolving the Black Hole Density Field

Fig. 1 illustrates several density evolution scenarios for accreting ( $\rho_{\bullet a}$ ) and quiescent ( $\rho_{\bullet q}$ ) black holes in our models. The remainder of this section describes our derivation of these histories.

In our framework, black-hole seeds form with a uniform mass  $m_\bullet^i$  in a fraction  $f_\bullet$  of newly collapsed halos up to a time

$t_{\max}^i$  (redshift  $z_{\min}^i$ ). We use the superscript ‘‘i’’ to denote that the masses are ‘‘initial’’.

Once a black-hole forms, we count its mass as contributing to  $\rho_{\bullet a}$  and let it grow exponentially with an e-folding (Salpeter) time of  $\tau_s$ . After an active lifetime of  $\tau_L$ , we assume that each black-hole stops growing/shining as a result of feedback and/or exhausting its fuel supply. At this point, we add its mass to  $\rho_{\bullet q}$ .

With these assumptions, we write down integral equations governing the evolution of  $\rho_{\bullet q}$  and  $\rho_{\bullet a}$  that we integrate numerically.

$$\rho_{\bullet a}(t) = m_{\bullet}^i \int_0^{\tau_L} \dot{n}_{\bullet} [t-t'] e^{t'/\tau_s} dt', \quad (9)$$

where

$$\dot{n}_{\bullet}(t) = f_{\bullet} \begin{cases} \frac{d}{dt} \int_{m_{\min}}^{m_{\max}} n_h(m, t) dm & t \leq t_{\max}^i \\ 0 & \text{otherwise} \end{cases} \quad (10)$$

and  $n_h(m, t)dm$  is the comoving number density of dark-matter halos with masses between  $m$  and  $m + dm$  at time  $t$ . The quiescent black hole density is given by

$$\dot{\rho}_{\bullet q}(t) = m_{\bullet}^i e^{\tau_L/\tau_s} \int_0^t \dot{n}_{\bullet}(t') dt' \quad (11)$$

While we choose to integrate in the time domain, our recipe for density evolution is functionally the same as the one used by Yue et al. (2013) to predict the contribution of black-holes to the high redshift infrared and X-ray backgrounds.

For our fiducial model, we consider a scenario in which black-holes form from massive Pop-III stars collapsing directly into black holes with  $m_{\bullet}^i = 10^2 M_{\odot}$  in 10% of halos (Hirano et al. 2015) with masses between  $T_{\text{vir}}^{\min} = 2000\text{K}$  and  $T_{\text{vir}}^{\max} = 10^4\text{K}$  (halo masses of  $m \approx 1.3 \times 10^6 M_{\odot} h^{-1}$  and  $m \approx 1.5 \times 10^7 M_{\odot} h^{-1}$  at  $z = 12$  respectively). We adopt a fiducial Salpeter time of

$$\tau_s = \frac{\tau_E \eta}{\lambda f_{\text{duty}}} \approx 45 \left( \frac{\eta}{0.05} \right) \left( \frac{1}{\lambda} \right) \left( \frac{0.5}{f_{\text{duty}}} \right) \text{Myr} \quad (12)$$

where  $\tau_E$  is the Eddington time-scale of 0.45 Gyr,  $\eta$  is the fraction of infalling rest-mass that is emitted as radiation,  $\lambda$  is the fraction of the Eddington luminosity that the black-hole radiates, and  $f_{\text{duty}}$  is the accretion duty cycle.

Accretion rates for black-hole seeds at  $z \gtrsim 10$  are, so-far, unknown. We settle on a fiducial value for  $\tau_s$  of 45 Myr, corresponding radiative efficiencies in the range of 0.025 – 0.1 (Shankar et al. 2010) and time-averaged Eddington ratios between 0.1 and 10, similar to what is observed at low redshift (Willott et al. 2010). We also employ a fiducial lifetime of  $\tau_L = 100\text{Myr}$ ; which is at the upper end of inferred accretion lifetimes observed at low-redshift (Bird et al. 2008; Shabala et al. 2008; Turner & Shabala 2015) but is consistent with accretion lifetimes in simulations of intermediate mass black-hole seeds growing in dense environments (Pacucci et al. 2015). We choose a fiducial minimum redshift for seed formation of  $z_{\text{seed}}^i = 16$ , which is within the range that Lyman-Werner regulated Pop-III formation has

Parameter	Description	Fiducial Value
$\tau_s$	black-hole mass e-folding time (Salpeter)	45 Myr
$\tau_L$	accretion lifetime	100 Myr
$z_{\min}^i$	minimum redshift for black-hole seed formation	16
$T_{\text{vir}\bullet}^{\min}$	minimum virial temperature of black-hole seed halos	2000 K
$T_{\text{vir}\bullet}^{\max}$	maximum virial temperature of black-hole seed halos	$10^4\text{K}$
$m_{\bullet}^i$	black-hole seed mass	$100 M_{\odot}$
$f_{\bullet}$	fraction of halos with seeds	$10^{-1}$

**Table 1.** Parameters associated with black-hole mass evolution and their ‘‘fiducial’’ values.

been found to cut off in semi-analytic studies (Mebane et al. 2017). Note that while seed formation ends at  $z_{\min}^i = 16$ , black holes continue to emit down to  $z \approx 12$  for our choice of parameters (Fig. 1). While we use the above ‘‘fiducial’’ values as reference points, our goal is to understand how specifically the signal changes when we vary them. We list our model’s parameters for black-hole growth along with their fiducial values in Table 1.

In order to build some intuition on equations 9 and 11, it is useful to inspect some general patterns in the density histories evolved with these equations (Fig. 1). ‘‘Small halos, fiducial accretion’’ corresponds to our fiducial model. We will discuss the specific deviations between each model in § 3.3. At early times, when  $t \lesssim \tau_s$ ,  $\rho_{\bullet a}$  grows proportional to  $\dot{\rho}_{\text{coll}}$  but quickly exceeds this growth after  $t \gtrsim \tau_s$ . New seeds stop forming after  $z_{\min}^i$ , causing  $\rho_{\bullet a}$  to turn over and fall to zero after  $t_{\max}^i + \tau_L$ . The ‘small halos, low- $z$ ’ line plateaus after  $z_{\min}^i$  but this is simply because the salpeter time and accretion lifetime (1 Gyr and 4.5 Gyr respectively) are much larger than the time interval on the plot. Quiescent densities remain at zero until  $\tau_L$  at which point they rapidly grow and flatten out at  $t_{\max}^i + \tau_L$  as the last accreting black holes die out and stop feeding the quiescent population.

In this work, we focus on the average black-hole density and its impact on the global 21 cm signal. However, our formalism can also be adopted into simulations of 21 cm fluctuations. One would simply track the black-hole density as a function of position by integrating equations 9 and 11 in each voxel using the spatially varying  $\dot{\rho}_{\text{coll}}$  instead of the global value, similar to what is done in the semi-numerical models 21cmFAST (M11) and simfast21 (Santos et al. 2008).

## 3.2 Radiation Backgrounds from Black Holes

We now describe our prescription for computing the radiative backgrounds from the black-hole mass density. These backgrounds include X-rays (§ 3.2.1), radio waves (§ 3.2.3), and UV photons (§ 3.2.2).

### 3.2.1 X-rays

X-ray emission from black-holes originates from three sources associated with accretion: thermal emission from the accretion disk, IC scattering of accretion disk photons off of hot electrons in the corona, and IC scattering of CMB photons by relativistic jet electrons.

Studies typically quantify the total X-ray luminosity of

Parameter	Description	Fiducial Value
$g_{\text{bol}}$	Accreted Mass emitted at 2-10 keV	$3 \times 10^{-3}$
$\alpha_X$	Spectral Index of X-ray emission	0.9
$N_{\text{H}}$	Hydrogen column depth	$3 \times 10^{23} \text{ cm}^{-2}$

**Table 2.** Parameters associated with X-ray emission and their fiducial values.

an AGN with the parameter  $k_{\text{bol}} \equiv L_{\text{bol}}/L_{[2-10]\text{keV}}$ . At low redshift, [Lusso et al. \(2010\)](#); [Marchese et al. \(2012\)](#) observe  $k_{\text{bol}}^{-1} \approx 0.06$  with X-ray emission dominated by IC upscattering of soft photons in the corona. AGN X-ray spectra usually exhibit an absorbed power-law with a spectral index of  $\alpha_X \approx 0.9$  ([Nandra & Pounds 1994](#)) and a high-energy exponential cutoff at 300 keV ([Titarchuk 1994](#)).

We set the amplitude of the time-averaged black-hole X-ray emissivity from the disk and corona through the accretion rate and a normalization parameter  $g_{\text{bol}} \cdot \int dE \epsilon_X(E) \propto g_{\text{bol}} \tau_s^{-1} \rho_{\bullet a}$ , where

$$g_{\text{bol}} \equiv 0.003 \left( \frac{\eta}{0.05} \right) \left( \frac{k_{\text{bol}}^{-1}}{0.06} \right). \quad (13)$$

We have included  $\eta$  in our definition of  $g_{\text{bol}}$  to cancel out the factor of  $\eta$  in  $\tau_s$  when these two variables are multiplied together.

Multiplying the bolometric accretion factor by an absorbed power-law and an exponential cutoff gives us our expression for the X-ray emissivity of black-holes,

$$\begin{aligned} \epsilon_{X\bullet}(E) \approx & 2 \times 10^{49} \left( \frac{45 \text{ Myr}}{\tau_s} \right) \\ & \times \left( \frac{g_{\text{bol}}}{0.003} \right) \left( \frac{A_{2,10}(\alpha_X)}{0.53} \right) \left( \frac{\rho_{\bullet a}}{10^4 M_{\odot} h^2 \text{ Mpc}^{-3}} \right) \left( \frac{E}{\text{keV}} \right)^{-\alpha_X} \\ & \times \exp[-(\sigma_{\text{HI}}(E) + \chi \sigma_{\text{HeI}}(E)) N_{\text{H}\bullet}] \\ & \times \exp(-E/300 \text{ keV}) \text{ keV s}^{-1} \text{ keV}^{-1} h^3 \text{ Mpc}^{-3}, \end{aligned} \quad (14)$$

where  $N_{\text{H}\bullet}$  is the Hydrogen column depth to the black-holes. In [Ewall-Wice et al. \(2018\)](#), we argued that the column depth necessary to explain an EDGES-like absorption feature with a duration of 100 Myr was roughly  $N_{\text{H}\bullet} \approx 10^{23.5} \text{ cm}^{-2}$ . In addition, simulations of direct collapse seeds often involve black holes growing in compton thick environments with  $N_{\text{H}\bullet} \gtrsim 10^{24} \text{ cm}^{-2}$  ([Yue et al. 2013](#); [Pacucci et al. 2015](#)) though it may be difficult for such column densities to be achieved for Pop-III seeds ([Alvarez et al. 2009](#); [Smith et al. 2018](#)). We adopt  $N_{\text{H}\bullet} = 10^{23.5} \text{ cm}^{-2}$  as a fiducial value but we will also explore much lower Hydrogen column depths.

### 3.2.2 UV and Optical Emission

UV emission affects the H I signal through Ly  $\alpha$  coupling and photo-ionizations. In accreting black-holes, UV photons are expected to arise from thermal disk-emission which is strongly correlated (through IC scattering) with coronal X-rays and usually follows a double power law with a transition at the Lyman limit. Additional emission arises through the reprocessing of absorbed UV and X-ray photons by obscuring gas. Our model includes both reprocessed and primary emission.

Parameter	Description	Fiducial Value
$\alpha_{OX}$	Optical-X-ray spectral slope	1.6
$\alpha_{O1}$	UV spectral slope	0.61

**Table 3.** Parameters associated with Optical emission and their fiducial values.

For primary emission from the accretion disk, we adopt the double power-law observed by [Lusso et al. \(2015\)](#) with  $\alpha_{O1} = -0.61$  for  $E \leq 13.6 \text{ eV}$  and  $\alpha_{O2}$  for  $200 \text{ eV} > E > 13.6 \text{ eV}$ . We set the overall UV amplitude through its correlation with X-ray emission (in radio quiete AGN),  $\epsilon_{X\bullet}(2\text{keV}) = \epsilon_{\text{UV}\bullet}(2500\text{\AA}) 10^{-\alpha_{OX}/0.384}$  and solve for  $\alpha_{O2}$  that is consistent with our choice of  $\alpha_{OX}$ . Combining the values observed in [Lusso et al. \(2010\)](#) and [Marchese et al. \(2012\)](#) with the unabsorbed  $\epsilon_{X\bullet}(2\text{keV})$  predicted by equation 14 gives us our expression for the UV emissivity of the black-holes,

$$\begin{aligned} \epsilon_{\text{UV}\bullet}(E) \approx & 7.8 \times 10^{52} \left( \frac{45 \text{ Myr}}{\tau_s} \right) \left( \frac{g_{\text{bol}}}{0.003} \right) \left( \frac{A_{2,10}(\alpha_X)}{0.53} \right) \\ & \times \left( \frac{\rho_{\bullet a}}{10^4 h^2 M_{\odot} \text{ Mpc}^{-3}} \right) \\ & \times 2^{0.9-\alpha_X} \left( 2.48 \times 10^{-3} \right)^{1.6-\alpha_{OX}} (2.74)^{0.61-\alpha_{O1}} \\ & \times \exp[-(\sigma_{\text{HI}}(E) + \chi \sigma_{\text{HeI}}(E)) N_{\text{H}\bullet}] \\ & \times \begin{cases} \left( \frac{E}{13.6\text{eV}} \right)^{-\alpha_{O2}} & E > 13.6 \text{ eV} \\ \left( \frac{E}{13.6\text{eV}} \right)^{-\alpha_{O1}} & E < 13.6 \text{ eV} \end{cases} \\ & \times \text{eV s}^{-1} \text{ eV}^{-1} h^3 \text{ Mpc}^{-3}. \end{aligned} \quad (15)$$

We list the parameters describing primary UV/Optical emission for our model in Table 3 along with their fiducial values.

The equivalent ionizing escape-fraction for black-hole, with column depth  $N_{\text{H}\bullet}$ , is  $f_{\text{esc}\bullet} = \int dE \epsilon_{\text{UV}\bullet} / \int dE \epsilon_{\text{UV}\bullet} \exp[(\sigma_{\text{HI}}(E) + \chi \sigma_{\text{HeI}}(E)) N_{\text{H}\bullet}]$  which is negligibly small for our fiducial column depths.

For secondary emission, we follow the prescriptions in [Yue et al. \(2013\)](#) and [Fernandez & Komatsu \(2006\)](#) in which considers Free-Free/Bound-Free continuum emission and two-photon emission from atoms excited by collisions and recombinations. We solve for the temperature of the obscuring gas following [Yue et al. \(2013\)](#), setting  $f_e = 0.5$  and balancing absorbed power from the black-holes primary spectrum with reprocessed power.

### 3.2.3 Radio

Radio emission from accreting black holes is observed from different phenomena associated with a relativistic jet: direct emission from the jet itself, which can be highly beamed, emission from compact regions such as hot-spots, and diffuse emission from lobes.

Total radio emission from AGN is often quantified relative to optical emission by a black-hole’s “radio loudness”,  $R$ , which often refers to the logarithm of the ratio between monochromatic 5 GHz and 2500 Å (primary) luminosities ([Kellerman et al. 1989](#)). We adopt the definition from [Ivezić et al. \(2002\)](#) where radio loudness is the log of the ratio between the observed 1.4 GHz and 8000 Å luminosities, translated to the mean redshift of the SDSS-FIRST sample

Parameter	Description	Fiducial Value
$\alpha_R$	Spectral Slope	1.1
$g_R$	Radio gain	3200

**Table 4.** Parameters associated with Radio emission and their fiducial values.

( $z \approx 1$ ). Since the mean redshift of the sample is  $z \approx 1$ . The resulting definition of  $R$  is the log-ratio between rest-frame 2.8 GHz and 4000 Å luminosities.

The nature and evolution of radio-loudness is not yet well understood. Some argue for two underlying populations of “radio quiet” AGN (with  $R \lesssim 0$ ) and “radio loud” AGN (with  $R \sim 3$ ) (Ivezić et al. 2002, 2004). Others contest that observations of bi-modality arise from selection effects (Cirasuolo et al. 2003; Singal et al. 2011). We refer to the fraction of sources that are radio loud as  $f_L$  and  $10^R$  as  $\mathcal{R}$ .  $\mathcal{R}$  and  $f_L$  might evolve significantly over time and there are tentative competing claims of constant, (Bañados et al. 2015), increasing (Donoso et al. 2009; Singal et al. 2011), and decreasing (Jiang et al. 2007) trends for  $f_L$  with redshift.

If the majority of radio loudness arises from diffuse lobes, then we might expect  $\mathcal{R}$  to be lower during the Cosmic Dawn due to IC losses off of the brighter CMB (Ghisellini et al. 2014). However, it is also possible that radio jets formed in environments with high densities and magnetic fields – allowing them to still radiate through the synchrotron channel.

We adopt the bi-modal radio-loudness distribution in Ivezić et al. (2002) between *rest-frame* 2.78 GHz and 4000 Å luminosities. For radio-loud sources,  $R$  is distributed as a Gaussian with a mean of  $\mu_R \approx 2.8$  and standard deviation  $\sigma_R \approx 1.1$ <sup>5</sup>

Since radio quiet AGN are typically  $\lesssim 10^3$  times fainter than their radio loud counterparts, we do not explicitly include them in our model. To quantify the radio-emission from our black-holes we introduce the parameter

$$g_R \equiv \frac{\epsilon_{\bullet}(2.8\text{GHz})}{\epsilon_{\bullet}(4000\text{Å})} = 3200 \times \left(\frac{f_L}{0.2}\right) \left(\frac{\langle \mathcal{R} \rangle}{1.6 \times 10^4}\right) \quad (16)$$

Adopting the Ivezić et al. (2002) distribution radio loudness yields  $\langle \mathcal{R} \rangle \approx 1.6 \times 10^4$ . We write down an equation for  $\epsilon_{R\bullet}$  by determining  $\epsilon_{UV\bullet}(4000\text{Å})$  from equation 15, multiplying by  $\langle \mathcal{R} \rangle$ , and scaling to 1 GHz. We choose a fiducial value for  $f_L$  of 0.2, the local radio loud fraction observed in the most luminous  $z \approx 0$  AGN.

$$\begin{aligned} \epsilon_{R\bullet}(v) \approx & 7.6 \times 10^{23} \left(\frac{g_R}{3200}\right) \left(\frac{g_{\text{bol}}}{0.003}\right) \left(\frac{A_{2,10}(\alpha_X)}{0.53}\right) \\ & \times 2^{0.9-\alpha_X} \left(2.48 \times 10^{-3}\right)^{1.6-\alpha_{OX}} \left(\frac{45\text{Myr}}{\tau_s}\right) \\ & \times (2.8)^{(\alpha_R-0.6)} (4.39)^{-(\alpha_{O1}-0.61)} \left(\frac{\rho_{\bullet,a}}{10^4 h^2 M_{\odot} \text{Mpc}^{-3}}\right) \\ & \times \left(\frac{v}{\text{GHz}}\right)^{-\alpha_R} \text{W Hz}^{-1} h^3 \text{Mpc}^{-3} \quad (17) \end{aligned}$$

<sup>5</sup> This is the distribution observed in (Ivezić et al. 2002) for rest-frame radio  $\approx 2.8$  GHz and optical  $\lambda \approx 4000$  Å.

### 3.3 Illustrative Scenarios

With our semi-analytic framework in place, we can now compute the global 21 cm signal under the influence of rapidly accreting radio-loud black hole seeds. Listing the parameters in our model (Table 5), we see that we are adding sixteen. An exhaustive exploration of the phenomenology of every one of these new parameter and their degeneracies is beyond the scope of this work. Instead, we investigate several different scenarios to illustrate the key dependencies of the signal morphology on halo and seed properties, obscuration and growth rate. We do so by focusing on  $\tau_s$ ,  $T_{\text{vir}\bullet}^{\text{min/max}}$ ,  $m_{\bullet}^i$ , and  $N_{\text{H}\bullet}$  we vary in the following models.

- **Small Halos:** Adopting all of the fiducial values discussed above, this model corresponds to Pop-III seeds arising in molecular cooling halos that are obscured by dense gas.

- **Large Halos:** A Scenario in which black holes form in halos above the atomic cooling threshold. We set  $T_{\text{vir}\bullet}^{\text{min}} = 1 \times 10^4$  K and  $T_{\text{vir}\bullet}^{\text{max}} = 5 \times 10^4$  K. The qualitative impact of larger halo masses is to move the absorption trough to later times.

- **Large Halos, Fast:** The same as our large halos scenario except that the accretion time-scale is lowered to 20 Myr. Lower  $\tau_s$  primarily increases the depth and side-steepness of the absorption feature while moving it to earlier times.

- **Large Halos, Unobscured:** The same as our large halos obscured scenario except that we lower the column densities to  $N_{\text{H}\bullet} = 10^{18} \text{cm}^{-2}$  which yields an equivalent black-hole UV escape fraction of 0.11. The primary qualitative effect of reducing  $N_{\text{H}\bullet}$  is to reduce the amplitude of the absorption trough through heating and ionizations.

- **Large Halos Massive Seeds:** We use this scenario to illustrate potential degeneracies that exist between  $m_{\bullet}^i$ ,  $\tau_L$  and  $\tau_s$ . In this model, the total energy radiated by a black hole over its lifetime is proportional to  $m_{\bullet}^f = m_{\bullet}^i e^{\tau_L/\tau_s}$  so we can approximately hold the amplitude of the total radio background constant by varying these three parameters in a way that holds  $m_{\bullet}^f$  constant. In our massive seeds model, we start with our fast model and raise  $m_{\bullet}^i$  to 1000  $M_{\odot}$  while increasing  $\tau_s$  to keep  $m_{\bullet}^f$  constant. The qualitative effect of increasing  $m_{\bullet}^i$  is similar to decreasing  $\tau_s$ .

- **Higher Obscuration:** Identical to our “large halos” scenario but now with the neutral column depth to black holes raised to  $N_{\text{H}\bullet} = 3 \times 10^{24} \text{cm}^{-2}$ .

- **Low-z Accretion:** A scenario where the accretion properties of the first black holes line up with what is observed in low redshift AGN. Specifically, we set  $\lambda = 0.1$ ,  $f_{\text{duty}} = 0.1$ , and  $\epsilon = 0.1$  (Shankar et al. 2010, 2013). This gives  $\tau_s = 4.5$  Gyr and  $g_{\text{bol}} = 0.006$ . We also adopt  $\tau_L = 1$  Gyr (Bird et al. 2008).

- **Stars :** A control scenario with no black holes,  $f_{\bullet} = 0$ .

We show the evolution of  $\rho_{\bullet,a}$  and  $\rho_{\bullet,q}$  in Fig. 1 for our various growth scenarios.  $\rho_{\bullet,a}$  leads  $\rho_{\bullet,q}$  until  $t_{\text{max}}^i$ , when the last black-hole seeds form. At  $t_{\text{max}}^i + \tau_{\text{fb}}$ , the last accreting black-holes shut down, bringing  $\rho_{\bullet,a}$  to zero and setting  $\rho_{\bullet,q}$  to a constant value. The onset of density growth is delayed depending on the minimum halo mass while  $\tau_s$  controls its steepness. The much larger accretion times of our low- $z$  models causes them to track the halo-collapse mass early on,

Scenario	Small Halos	Large Halos	Large Fast	Un- Obscured	Massive Seeds	Highly Obscured	Low-z Accretion	Stars Only	EDGES Small Halos	EDGES Large Halos
$\tau_s$ (Myr)	45	45	20	45	45	45	$10^3$	-	25	18
$\tau_L$ (Myr)	100	100	100	100	100	100	100	-	100	100
$z_{\min}^i$	16	16	16	16	16	16	16	-	21	21
$T_{\text{vir}\bullet}^{\min}$ (K)	2000	$10^4$	$10^4$	$10^4$	$10^4$	$10^4$	$10^4$	-	2000	$10^4$
$T_{\text{vir}\bullet}^{\max}$ (K)	$10^4$	$5 \times 10^4$	$5 \times 10^4$	$5 \times 10^4$	$5 \times 10^4$	$5 \times 10^4$	$5 \times 10^4$	-	$10^4$	$5 \times 10^4$
$m_{\bullet}^i$ ( $M_{\odot}$ )	100	100	100	100	1000	37	100	-	100	1500
$f_{\bullet}$	0.1	0.1	0.1	0.1	0.1	0.1	0.1	-	0.1	0.1
$g_{\text{bol}}$	0.003	0.003	0.003	0.003	0.003	0.003	0.003	-	0.001	0.001
$\alpha_{X\bullet}$	0.9	0.9	0.9	0.9	0.9	0.9	0.9	-	0.5	0.5
$N_{\text{H}\bullet}$ ( $\text{cm}^{-2}$ )	$3 \times 10^{23}$	$3 \times 10^{23}$	$3 \times 10^{23}$	$10^{18}$	$3 \times 10^{23}$	$3 \times 10^{24}$	$3 \times 10^{23}$	-	$1.8 \times 10^{24}$	$3 \times 10^{24}$
$\alpha_{OX}$	1.6	1.6	1.6	1.6	1.6	1.6	1.6	-	1.6	1.6
$\alpha_{O1}$	0.61	0.61	0.61	0.61	0.61	0.61	0.61	-	0.61	0.61
$\alpha_R$	1.1	1.1	1.1	1.1	1.1	1.1	1.1	-	1.1	1.1
$\mu_R$	2.8	2.8	2.8	2.8	2.8	2.8	2.8	-	2.1	2.1
$\sigma_R$	1.1	1.1	1.1	1.1	1.1	1.1	1.1	-	1.1	1.1
$f_L$	0.2	0.2	0.2	0.2	0.2	0.2	0.2	-	1	1

**Table 5.** Values for the Black-Hole growth and emission parameters for all models explored in this work. The parameter choice for “Small Halos” corresponds to our “fiducial” model.

which is why our “low-z” and “small halos” models agree at  $t \lesssim 0.125$  Gyr. All of the models considered produce black-hole densities below the  $z \sim 0$  limits of  $\lesssim 10^6 h^2 M_{\odot} \text{Mpc}^{-3}$  established by dynamical studies (Merritt & Ferrarese 2001). As we might expect, our “massive seeds” and “fast” models produce the same quiescent mass densities, which are set by  $m_{\bullet}^f$  and their identical halo properties (equation 11). The evolution of accreting densities do differ with the “massive seeds” scenario assembling more accretion mass earlier on and with the “fast” scenario catching up through its faster growth rate.

## 4 MODELING RESULTS

We now discuss the results of our global signal calculation.

### 4.1 The Brightness Temperature and Thermal Evolution

We start our discussion with plots of  $\delta T_b$  in the top left panel of Fig. 2 and compare its timing with the evolution of  $T_r$ ,  $T_k$ , and  $T_s$  in the other panels. We show the evolution of  $\delta T_b$ , under the influence of stars only, as a dashed orange line in the top left panel of Fig. 2. Without black holes,  $\delta T_b$  follows the canonical evolution observed in most theoretical models with an absorption trough initiated by Ly  $\alpha$  coupling of the spin temperature to the kinetic temperature of the adiabatically cooled H I gas and ended by X-ray heating which drives the H I into emission before ionization brings  $\delta T_b$  to zero.

All of our models that involve obscured black-holes yield a feature that is significantly deeper and narrower than our stellar model (Fig. 2, top left, excluding the black dotted, blue dashed, and orange dashed lines). Many of the scenarios, which either involve greater obscuration or enhanced black hole densities, extend beyond the  $\sim 250$  mK limit that is expected without a radio background (top left purple/pink dot-dashed and solid black lines).

Comparing scenarios with large (all lines but orange dashed) and small (thick black line) halos, one sees that raising the minimum halo virial temperature causes an overall

delay in the evolution of  $\delta T_b$ . We see that the Small Halos model, which roughly corresponds to SMBH progenitors forming from Pop-III seeds, predicts an absorption trough that is too early to explain the EDGES observation. This is consistent with Kaurov et al. (2018)’s conclusion that the timing of the EDGES trough suggests Ly  $\alpha$  coupling and heating driven by massive halos. However, a 100 Myr delay between Pop-III seed formation and accretion, which has been predicted by some models (Johnson & Bromm 2007), can shift the feature such that the timing of the absorption feature agrees with EDGES.

While our choice of  $\alpha_R = 1.1$  is motivated by calculations of Synchrotron cooling times during the Cosmic Dawn (Sharma 2018), we look into the consequences of a flatter spectral index by plotting models with  $\alpha_R = 0.5$  as light lines in Fig. 2. By reducing the rest-frame emission below 2.8 GHz, flatter spectral indices tend to reduce the radio backgrounds and absorption amplitudes in our models.

The contrast between our Large Halos (dotted blue) and Large Halos Fast (purple dot dashed) models illustrates how  $\tau_s$  affects the steepness of the absorption feature’s sides. Smaller  $\tau_s$  corresponds to a deeper and narrower trough due to faster Ly  $\alpha$  coupling, heating, and radio emission. We illustrate the higher rate in evolution that results by plotting the derivative of  $\delta T_b$  with respect to frequency in Fig. 3.

Inspecting the up-turn at  $z \sim 17$  in the evolution of  $T_k$  and  $T_s$  in the top-right and bottom-left panels of Fig. 2, we see that the Ly  $\alpha$  emission from black holes and stars only partially couples the spin temperature to  $T_k$  at its minimum. Full coupling of  $T_s$  to  $T_k$  does not happen until substantial X-ray heating has already occurred.

The brightness temperature evolution for our Massive Seeds (thin black line) and Fast (purple dot-dashed line) models are very similar since both radiate equal amounts of energy per co-moving volume. However, the Massive Seeds scenario shifts the total brightness evolution to slightly earlier times since more massive seeds result in more mass being assembled at earlier times than the Fast model, even if both scenarios eventually assemble the same black hole mass. Increasing the obscuration of black holes to reduce and delay heating is another way of increasing the total ab-



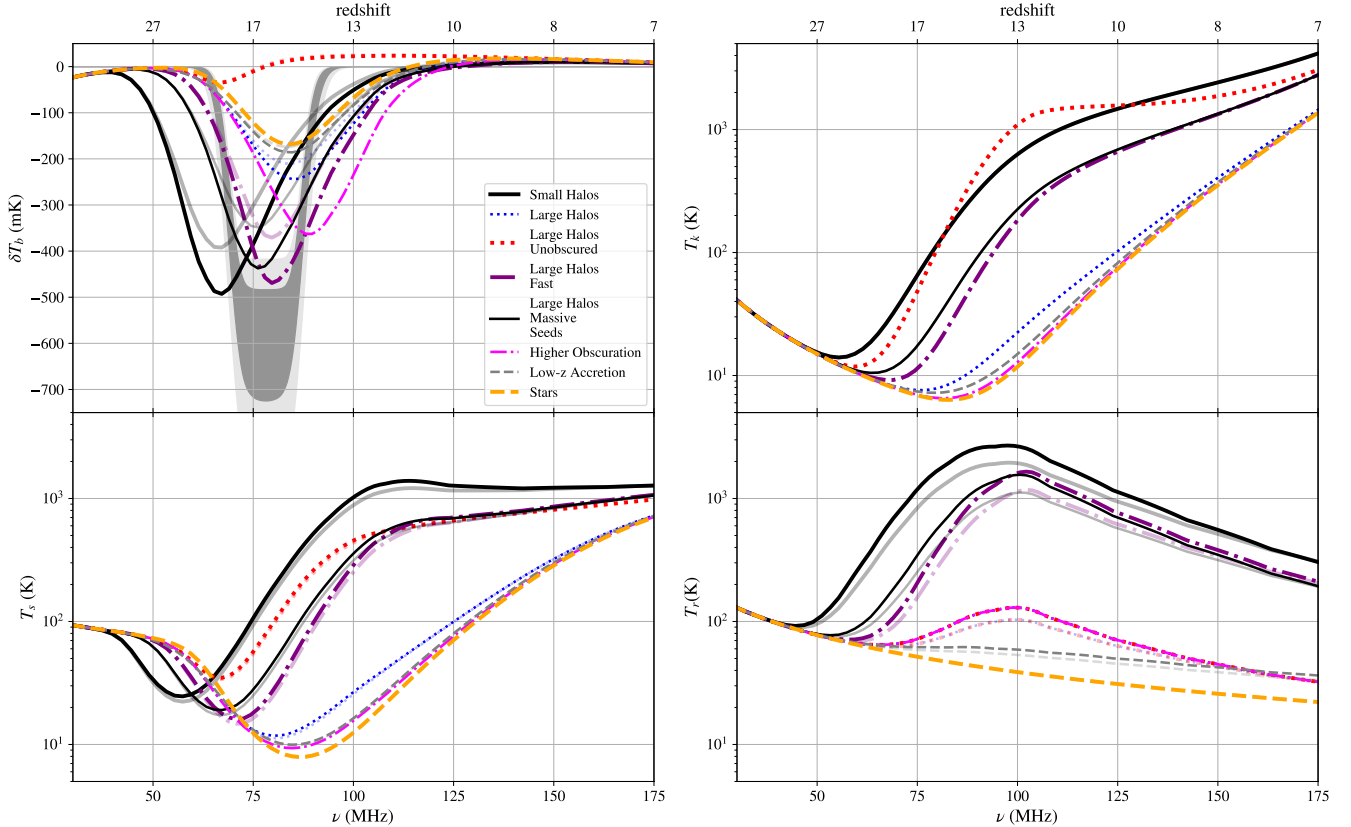


**Figure 2.** The evolution of the 21 cm brightness temperature,  $\delta T_b$  (top left), the radio background temperature,  $T_r$  (bottom right), the H I kinetic temperature,  $T_k$  (top right), and the H I spin temperature,  $T_s$  (bottom left) in our simulations. A model without black-holes (orange dashed line) exhibits the canonical global signal evolution. Parameters for other models are listed in Table 5. The grey shaded region shows  $1\sigma$  and  $2\sigma$  contours for the EDGES detection. Models with black holes introduce a deeper and narrower absorption trough that drops below the  $\sim 250$  mK limit for adiabatically cooling gas absorbing the CMB from recombination. Increasing the minimum halo mass delays the onset of heating, resulting in an overall translation of the global signal (compare thick black and dotted blue or pink/purple dot dashed lines). Decreasing  $\tau_s$  increases the heating and reionization rates, causing the sides of the trough to steepen. Increasing the seed mass both increases the trough depth and translates it to earlier times. The Small Halos (thin black line) model predicts an absorption feature that is too early to explain EDGES although a 100 Myr delay between seed formation and accretion can relieve this tension. Light lines denote models where the radio spectral index is flattened from 1.1 to 0.5.

sorption depth. Comparing the Higher Obscuration (pink dot dashed), Massive Seeds (thin black), and Fast (purple dot-dashed line) curves in Fig. 2, we see that increasing the obscuration depth also moves the trough to lower redshifts (the opposite effect of Massive Seeds).

Comparing  $T_k$  and  $\delta T_b$  for all of our models (Fig. 2), we see that the absorption minimum occurs after some X-ray heating has already taken place and  $T_r$  is within a factor of a few of the CMB value. V18 find an order 10% change in  $\delta T_b$  from radio heating for a radio background that is  $3.5\times$  the CMB value with no X-ray heating. Since the gas in our model experiences similar CMB levels in addition to X-ray heating, we conclude that the V18 effect has a  $\lesssim 10\%$  impact on the amplitudes of our predicted absorption amplitudes.

All of our black-hole scenarios accelerate the global-signal’s evolution beyond the stellar scenario. This is primarily due to the fact that the black-hole emissivities, through exponential growth and large seed masses, can outpace the time-evolution of stellar emissivities which are limited by the halo-collapse rate.

## 4.2 Ionization Histories

Fig. 4 shows the ionization histories of our models. All are very similar though the reionization produced by our “unobscured” model is slightly more rapid. To get a sense of how our models line up against existing constraints, we show the  $2\sigma$  region from Greig & Mesinger (2017) which is derived by fitting a popular three-parameter model to observations of the CMB and quasar spectra. We also show the  $2\sigma$  contours from the model-independent principal component (PC) analysis of Planck Collaboration et al. (2016) data derived by Millea & Bouchet (2018). All of our models are consistent with the Millea & Bouchet (2018) and Greig & Mesinger (2017) constraints.

## 4.3 Local Backgrounds

How do cosmological backgrounds vary across our models? In Fig. 5, we plot the radio monopole observed at  $z = 0$  as a result of our black hole models and compare them to various measurements (Seiffert et al. (2011) and references

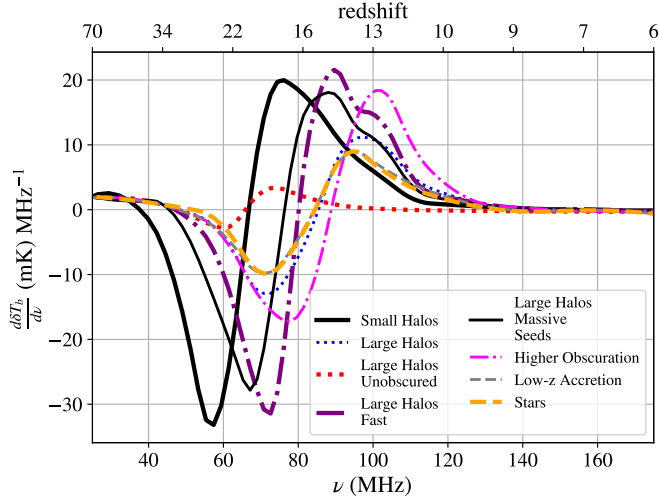


**Figure 3.** The derivative of  $\delta T_b$  with respect to frequency. Comparing the Large Halos and Fast models we see that the steepness of the rising and falling sides of the sides of the absorption feature are increased with decreasing  $\tau_s$ .

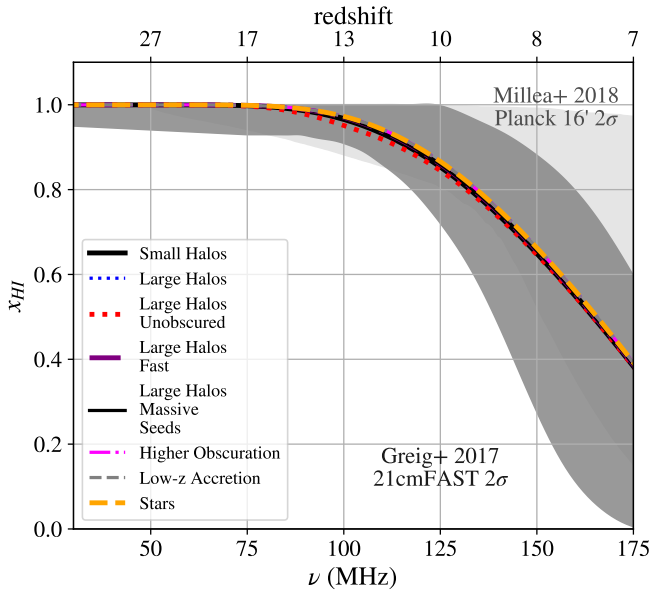


**Figure 4.** The evolution of the neutral fraction,  $x_{\text{HI}}$ . We include the 21cmFAST derived  $2\sigma$  contours from Greig & Mesinger (2017) (dark grey contours) along with the PC derived constraints from Millea & Bouchet (2018) (light grey contours).

therein). As one might expect, the models that achieve a larger absorption trough by increasing co-moving radio emissivity also result in the largest backgrounds. Since “massive seeds” (thin black line) and “fast” (purple dot dashed line) models both radiate the same amount of energy in the radio so their aggregate backgrounds are practically identical. This is despite the fact that the “massive seeds” model yields a slightly earlier trough (Fig. 2). Since they involve identical black hole masses and primary emission properties,

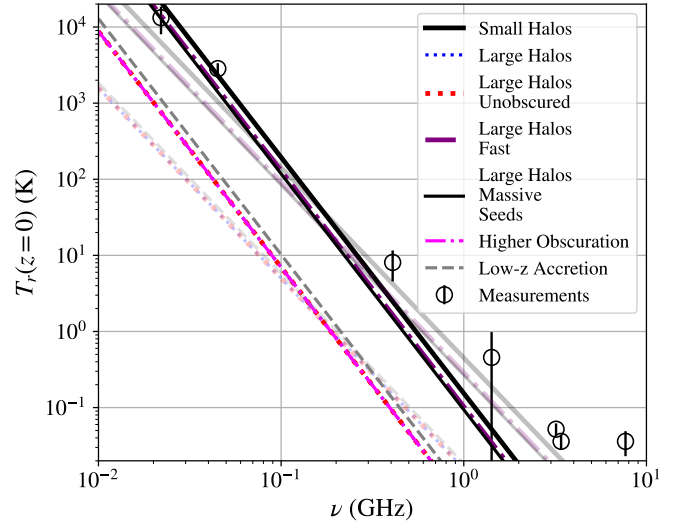


**Figure 5.** The radio-background predicted for our models as a function of frequency compared (various lines) to measurements of the radio monopole with point sources subtracted (black circles). The models that we consider produce radio-backgrounds that are below or consistent with existing constraints. Light lines denote the same models as the dark lines but with a flatter spectral index ( $\alpha_R = 0.5$ ). We do not include our Stars Only model in this plot since it does not produce any radio emission.

the “Large Halos”, “Unobscured”, and “Higher obscuration” models also produce identical radio backgrounds and very different absorption signatures. We note that at the column depths considered, obscuring gas only has a small impact on radio propagation (Ewall-Wice et al. 2018).

We also compute the soft X-ray background (XRB) for each model which we plot in Fig. 7. The disparate obscuration depths for XRBs and AGN yield a distinctive peaked structure at low energies. Since high obscuration of AGN is required to explain the EDGES feature, limits on any double peaked nature of the Cosmic Dawn XRB might help validate or constrain black-hole accretion as an explanation. The amplitude trends noted in the radio backgrounds hold the same for X-rays except for the absence of an obscuration related cutoff since varying  $N_{\text{HI},\bullet}$  does not affect the emergent radio spectrum. We compare predicted XRBs to the  $\sim 2.5 \times 10^{-13} \text{ erg s}^{-1} \text{ cm}^{-2} \text{ deg}^{-2}$  upper limit on the 0.5–2 keV unresolved extra-galactic XRB determined by Cappelluti et al. (2013); Fialkov et al. (2017) and find that none of our models exceed this limit.

#### 4.4 The Impact of Radio Loudness on the Global 21 cm Signal

We examine the level that the radio-loudness of AGN impacts  $\delta T_b$  as a first attempt to understand at what level 21 cm global-signal measurements might constrain the existence of radio loud accretion during the Cosmic Dawn. In Fig. 6, we compare  $\delta T_b$  for our black-hole scenarios with  $f_L = 0$  and  $f_L = 0.2$ . While radio-emission has little impact on scenarios dominated by unobscured black-holes, its impact on obscured models ranges from tens to hundreds

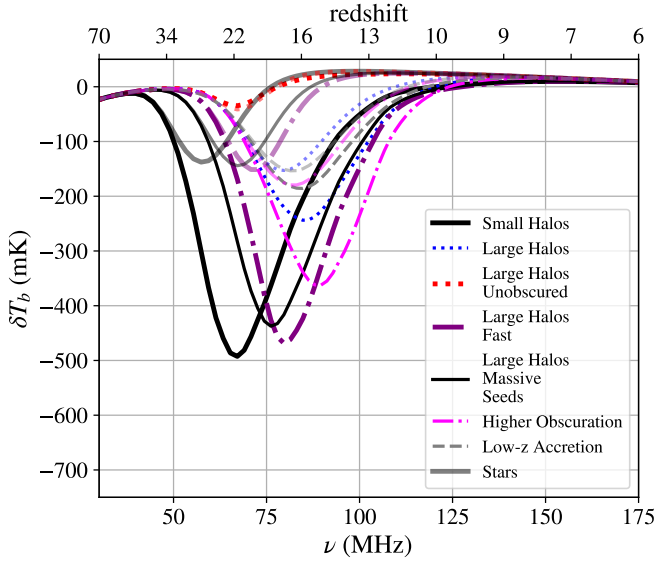


**Figure 6.** The 21 cm brightness temperature for our various black-hole scenarios with a radio fraction of  $f_L = 0.2$  (dark lines) and  $f_L = 0.0$  (light lines). In scenarios with high accretion rates, the 21 cm signal arising from obscured black-holes can be impacted at the hundreds of percent level. Radio-loudness can have a  $\sim 10\%$  impact (grey dashed lines) even when black-hole seeds experience accretion rates similar to what is observed at low redshifts.

of percent; even when the accretion rates and duty cycles are at relatively low levels. It is therefore important to include the impact of radio emission when the 21 cm signal is heavily impacted by the growth of black hole seeds, such as those considered by Zaroubi et al. (2007) and Tanaka et al. (2016). When a fraction of AGN ( $\sim 10\%$ ) are radio loud, the trough appears deeper and later than it would otherwise (compare dark and light sets of lines). It is likely that lower levels of accretion will be degenerate with other astrophysical signatures but should be included to account for such degeneracies.

While an absorption trough that is deeper than the adiabatic minimum would be suggestive of excess radio emission, it is unclear whether the differences caused by radio emission can be disentangled from other astrophysical effects when this is not the case.

#### 4.5 Source Counts

We compute radio-source counts to determine whether upcoming surveys might be used to test our models and help lift degeneracies in the global signal. In Fig 8, we show the contribution of sources per decade of flux towards the total background intensity which can be written as  $dn/dS^2$  where  $dn/dS$  is the differential number of sources per unit solid angle and unit flux.

To understand how much of the scatter in source fluxes arises from the width of the radio loudness distribution, we also compute  $S^2 dn/dS$  when the radio-loudness distribution is a delta-function at the loudness that gives the same comoving emissivity as the usual log-normal (Fig. 9). Such

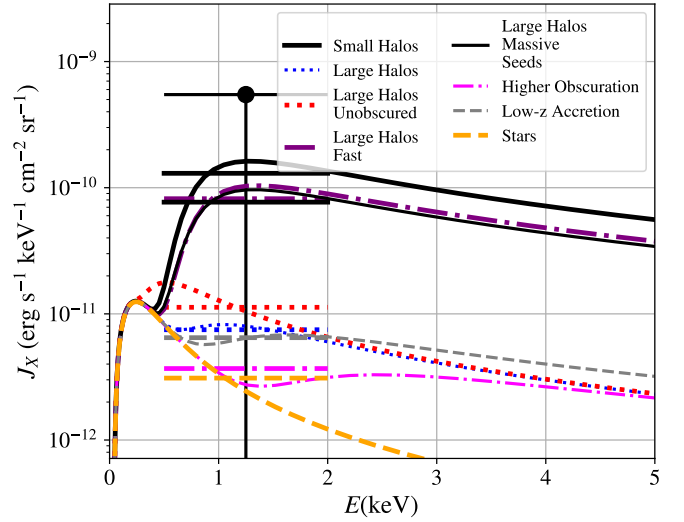


**Figure 7.** The soft XRB arising from our various global signal models described in § 3.3. Obscured models agree well with their unobscured counterparts at high X-ray energies (compare red dotted and blue dotted lines). The black point indicates the upper limit on the unresolved extra-galactic background implied by Chandra deep field limits between 0.5 and 2 keV. Horizontal lines are the average brightness over 0.5 – 2 keV for each model. The large obscuring column depths required for AGN to explain EDGES imprint a distinctive double-peaked Cosmic Dawn XRB where the low energy peak arises from less obscured X-ray binaries.

Name	Frequency	5- $\sigma$ threshold	Area
LOFAR	150 MHz	30 $\mu$ Jy	All-Sky
MIGHTEE-1	1.4 GHz	20 $\mu$ Jy	10 <sup>3</sup> deg <sup>2</sup>
MIGHTEE-2	1.4 GHz	5 $\mu$ Jy	20 deg <sup>2</sup>
SKA1-DEEP	1.4 GHz	1 $\mu$ Jy	10 deg <sup>2</sup>
SKA1-ULTRADEEP	1.4 GHz	0.1 $\mu$ Jy	1 deg <sup>2</sup>
VLA3-3	3 GHz	10 $\mu$ Jy	10 deg <sup>2</sup>

**Table 6.** The properties of upcoming radio-surveys forecasted by P15

a delta distribution would be practically indistinguishable from the log-normal in mean background measurements. We find that eliminating the spread in radio-loudness significantly tightens up the radio flux distributions while the flux distribution peaks remain the same.

We also examine flux distributions for a shallower spectral index of  $\alpha_R = 0.5$  (light lines in Figs. 8 and 9). While our steep spectrum is motivated by predictions for synchrotron aging (Sharma 2018), a spectral index of 0.5 is more consistent with the ARCADE-2 excess. A shallower spectral index results in higher source counts at  $\gtrsim$  GHz frequencies.

While the “Large Halos Fast”, “Massive Seeds”, and “Small Halos” models yield very similar total intensities (Fig. 5), they are highly separated in Fig. 8 and Fig. 9. Specifically, these models have very different peak fluxes. This is because the maximum source luminosity is proportional to  $\tau_s^{-1} m_{\bullet}^i e^{\tau_s/\tau_L}$ . This quantity is lowered in the “Massive Seeds” model which at the same time has the same  $m_{\bullet}^i e^{\tau_s/\tau_L}$  and larger  $\tau_s$ .

A number of our models, while allowed in background measurements, are eliminated by existing limits on point source populations. To illustrate this, we plot the  $2 - \sigma$  regions allowed by recent fluctuations analyses at 1.4 GHz (Condon et al. 2012) (C12) and 3 GHz (Vernstrom et al. 2014) (V14). When wide radio-loud distributions are present, their high flux tails tend to conflict with existing limits if most  $\sim 10\mu\text{Jy}$  are indeed SFGs (and potentially confuse interpretations if these sources are not). For narrow radio loudness distributions, the Fast and Massive Seeds models discussed here are still ruled out while the other scenarios are allowed since they concentrate a large number of sources below the thresholds of current fluctuation analyses.

To determine the detectability of Cosmic dawn black holes in future radio surveys, we also show the flux-sensitivities of upcoming experiments from Shimwell et al. (2017) and Prandoni & Seymour (2015) (P15) in Figs. 8 and 9. These sensitivities take into account thermal noise and the confusion limit of known power-law distributions of sources. We have found that the contributions of the black holes to confusion noise to be negligible in comparison.

Planned deep surveys on the mid band SKA 1 (SKA1-MID) will resolve the flux peaks of models producing an EDGES level feature with sources located in atomic cooling halos, but not necessarily the scenarios with small Pop-III black holes in molecular cooling halos. While it may not be possible to resolve individual sources in these models, fluctuation analyses might still be used to constrain scenarios driven by fainter  $\lesssim \mu\text{Jy}$  populations.

All of the models that we examine that produce an EDGES level feature also introduce a substantial  $\sim \mu\text{Jy}$  source population. However these sources can, in principal, be moved to smaller (and more numerous) halos in exchange for smaller fluxes.

The minimum halo mass hosting a black hole can be used to set a characteristic flux for sources that produce a radio background with temperature  $T_{\text{ref}}$  at redshift  $z_{\text{ref}}$  and frequency  $\nu_{\text{ref}}$ . For an order-of-magnitude calculation, we assume that all of our radio sources have equal luminosity, occupy  $f_{\text{halo}}$  of dark-matter halos between  $T_{\text{vir}}^{\text{min}}$  and  $T_{\text{vir}}^{\text{max}}$ , and exist up to redshift  $z_{\text{min}}$ . To generate a radio background of  $T_{\text{ref}}$  at  $z_{\text{ref}}$ , their distribution must be overved at  $z = 0$  to include sources with fluxes of at least

$$S_{\nu_{\text{obs}}}^{\text{min}} = \frac{2k_B T_{\text{ref}}}{\lambda_{\text{ref}}^2 (1 + z_{\text{ref}})^{1+\alpha_R}} \left( \frac{\nu_{\text{obs}}(1 + z_{\text{min}})}{\nu_{\text{ref}}} \right)^{-\alpha_R} \times \left[ c D_L^2(z_{\text{min}}) \int_{z_{\text{min}}}^{\infty} \frac{n(z') dz'}{H(z')(1 + z')^{1+\alpha_R}} \right]^{-1}. \quad (18)$$

In reality, the luminosities of black holes should increase with time so that the most luminous sources appear at lower redshifts with even larger fluxes. Hence, we can consider the characteristic flux obtained from equation 18 as an order of magnitude lower bound on source fluxes required to produce  $T_{\text{ref}}$ .

To produce the EDGES feature, the radio background must at least be as bright as  $T_{\text{ref}} \gtrsim 2.73\text{K}(1 + z_{\text{min}})$  at  $\nu_{\text{ref}} \approx 1.4\text{GHz}$  with  $z_{\text{min}} = z_{\text{ref}} = 17$ . Plugging these numbers into equation 18, we obtain lower limits on flux densities in Fig. 8 which we denote with vertical dotted black lines for “large” and “small” halos. We see that producing the

EDGES excess with atomic cooling halos requires a population of sources with  $S \sim 10^{-2}\mu\text{Jy}$  at GHz frequencies while if molecular cooling halos hosted the same sources, the characteristic fluxes of these sources is on the order of  $S \sim \text{nJy}$ . From the dashed green lines, source fluxes to produce the ARCADE-2 excess at 3 GHz require a population of  $\sim 10^{-1} - 10^1 \text{Jy}$  sources at  $\sim 1.4\text{GHz}$ . Since most of our scenarios produce radio-backgrounds similar to ARCADE-2, they simultaneously give rise too source populations with characteristic fluxes within an order of magnitude of our predictions. While these characteristic fluxes are sensitive to our choice of spectral index (1.1), and the specific fraction of halos hosting black holes (we chose 10%) they serve as an order of magnitude estimate of what sort of fluxes we should expect from radio surveys if EDGES or ARCADE-2 are produced by discrete sources with one source per halo.

## 5 CAN RADIO LOUD BLACK HOLES EXPLAIN EDGES?

The 21 cm absorption feature described in B18 has several unusual characteristics that are difficult to explain with models driven solely by stellar backgrounds. These features include

- (i) A large depth of  $\sim 500 \text{mK}$
- (ii) A narrow width of  $\Delta z \lesssim 10$ .
- (iii) Steep sides that climb  $500 \text{mK}$  over  $\Delta z \lesssim 2$
- (iv) A flat bottom.

In Fig. 2, we compare our models to the 68% and 95% confidence regions derived from the MCMC fit of the raw EDGES data between 60 – 94 MHz published by B18<sup>6</sup>. None of our models agrees well with the EDGES signal though our Fast and Massive Seeds models best reproduce the steepness and timing of the EDGES trough though they are still far less steep.

Guided by the intuition built in § 4, we obtain a better fitting model from our Small Halos scenario by reducing the Salpeter time to  $\sim 18.2 \text{Myr}$ , delaying the trough by adding a 60 Myr delay between seed formation and vigorous accretion, and trading off the radio luminosity of each source for a greater number of sources by setting  $g_{\text{bol}} = 0.001$ ,  $f_L = 1$ , and  $\mu_R = 2.1$ . The adjustments to the source radio properties yield a similar radio gain to our fiducial model while better satisfying source count constraints by reducing the flux of each source.

We finally make fine adjustments to better match the trough by increasing the Hydrogen column depth to  $1.8 \times 10^{24} \text{cm}^{-2}$ , reducing  $T_{\text{vir}}^{\text{min}}$  to 1000 K, raising  $z_{\text{min}}^i$  to 21.5, and reducing  $\alpha_X$  to 0.5.

With these adjustments, we obtain a model that agrees roughly with the EDGES contours which we show in Fig. 10. In Tables 5 and 7, we list these parameters that approximately fit the EDGES signal as EDGES Small Halos.

Since it is difficult to obscure black holes in molecular cooling halos, we obtain a similar EDGES-like model with atomic cooling halos by starting with the EDGES Small

<sup>6</sup> <http://loco.lab.asu.edu/EDGES/EDGES-data-release/>

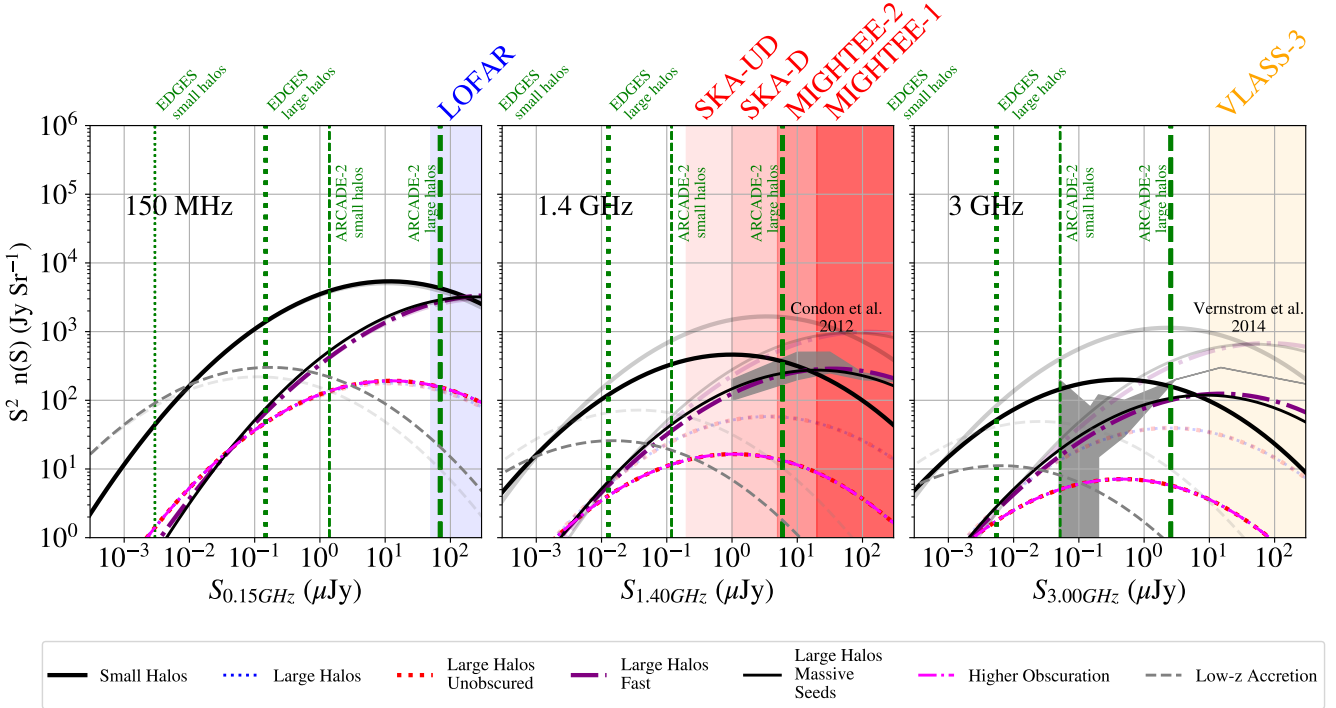


**Figure 8.** Intensity per logarithmic flux-bin for our various black-hole models. The grey shaded regions denote constraints derived from the confusion analyses by C12 at 1.4 GHz and V14 at 3 GHz which exclude the Small Halos Fast model due to its large number of predicted sources. We note that this would not be the case for a tighter radio loudness distribution (Fig. 9). Since the Fast and Massive Seeds models produce most of the observed source counts between  $1 - 10 \mu\text{Jy}$ , they may be in tension and/or are degenerate with contributions from SFGs. While the Fast, and Massive Seeds scenarios predict similar radio backgrounds, their flux distributions are quite different. Thus, radio surveys are helpful in removing degeneracies that exist in observations of  $\delta T_b$  alone. Fluctuation analyses and expected SFG counts already constrain the Small Halos, Fast, and Massive Seeds models. We do not include the Stars model in this plot since it does not produce any radio point sources. The projected  $5\sigma$  point-source detection thresholds of point-source surveys by the SKA1, LOFAR, and the VLA calculated in P15 are denoted by colored shaded regions. Green vertical lines denote the characteristic fluxes of sources that can explain the ARCADE-2 (vertical dashed green lines) and EDGES (vertical dotted green lines) detections. Transparent sets of lines show models where the spectral index has been flattened from 1.1 to 0.5. Flatter spectrum scenarios are generally more constrained than their steep spectrum counterparts.

Halos model, increasing the temperature range of seed halos to between  $T_{\text{vir}\bullet}^{\text{min}} = 10^4 \text{ K}$  and  $T_{\text{vir}\bullet}^{\text{max}} = 5 \times 10^4 \text{ K}$ , the seed mass to  $1500 M_{\odot}$ , and the neutral column depth to  $N_{\text{HI}\bullet} = 3 \times 10^{24} \text{ cm}^{-2}$ . Our large halos model involves fewer halos by making each individual black hole  $\gtrsim 10\times$  brighter than in the Small Halos scenario. In doing so, it begins to brush up against constraints at  $S \gtrsim 1 \mu\text{Jy}$  derived from confusion (Fig. 14). By increasing  $N_{\text{HI}\bullet}$ , we achieve the EDGES amplitude without violating confusion constraints.

We find two significant disagreements between our models and the EDGES signal that we are not able to mitigate through choosing “better” parameters. Firstly,  $\delta T_b$  flattens out more gradually at  $z \approx 14$ , extending the end of the absorption feature beyond what the nominal EDGES detection. One way to reduce this flattening is to enhance the ionizing efficiency of SFGs by increasing  $f_{\text{esc}}$  to unity and  $N_{\gamma\star}$  to  $10^4$ . We show these fast ionization models as lightly colored lines in Fig. 10. Without raising the difficulties in achieving such a large ionizing flux, significant ionization at  $z \approx 14$  would be in tension with other probes (Fig. 12). Secondly, none of our models appears to have a flattened bottom.

We compare the X-ray and radio backgrounds from our EDGES-like models to existing limits in Figures 13 and 11. We also show the source count distributions in Figs. 14. By construction, our Small Halos model lies just within existing radio-background constraints though the background amplitude might be made lower by increasing the obscuration of the black-holes. The XRB is similarly, thanks to obscuration, just below Chandra upper limits. Since our Large Halos model yields a population of  $\gtrsim \mu\text{Jy}$  sources that are constrained by confusion analyses, we do not have the freedom to produce such a strong radio background. Both the X-ray and radio backgrounds for the Large Halos model are well below that of Small Halos and limits in the literature.

To summarize, our model can explain the large depth and steepness of the EDGES feature. In order to be consistent with  $\mu\text{Jy}$  confusion analyses, models that involve halos above the atomic cooling limit are required to increase obscuration in order to preserve a large absorption amplitude and generate smaller fractions of the observed radio and X-ray backgrounds.

Our model is not able to reproduce the flat-bottom of the trough observed by B18 and in order to explain the rapid

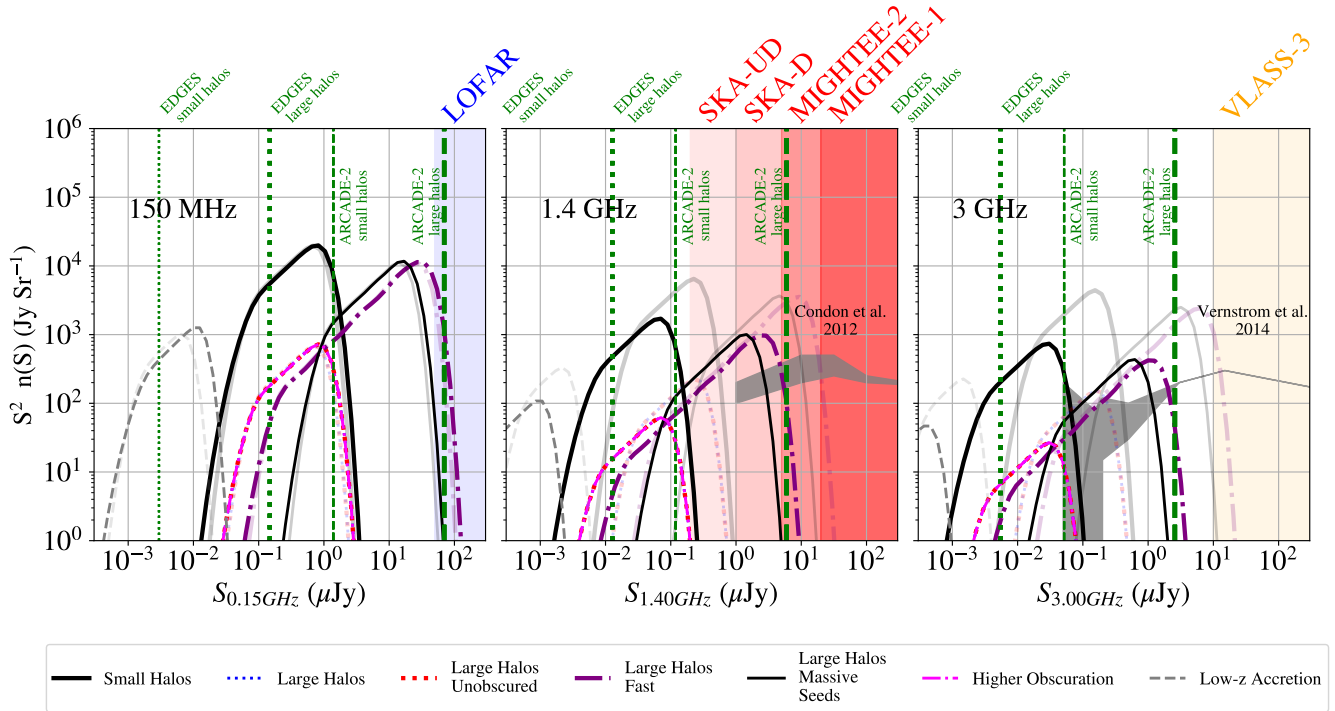


**Figure 9.** The same as Fig. 8 but now collapsing the log-normal radio loudness distributions into delta functions that yield the same mean co-moving radio emissivity. This removes the high flux tails in Fig. 8 and increases the number of sources at the distribution peaks. This trade-off allows for models involving molecular cooling halos to skirt below (albeit in a contrived way) the C12/V14 constraints.

Parameter	EDGES small halos	EDGES large halos
$T_{\text{vir}\bullet}^{\text{min}}$	$1 \times 10^3$ K	$1 \times 10^4$ K
$T_{\text{vir}\bullet}^{\text{max}}$	$1 \times 10^4$ K	$5 \times 10^4$ K
$m_{\bullet}^i$	$100 M_{\odot}$	$1500 M_{\odot}$
$\tau_d$	60 Myr	100 Myr
$\alpha_{X\bullet}$	0.5	0.5
$N_{\text{HI}\bullet}$	$1.8 \times 10^{24} \text{ cm}^{-2}$	$3 \times 10^{24} \text{ cm}^{-2}$
$\tau_s$	25 Myr	18 Myr
$z_{\text{min}}^i$	21.5	21.5
$f_L$	1.0	1.0
$\mu_R$	2.1	2.1
$g_{\text{bol}}$	0.001	0.001

**Table 7.** Parameter values for two models that are in approximate agreement with the EDGES detection (shown in Fig. 10). A smaller  $\tau_s$  and larger  $T_{\text{vir}\bullet}^{\text{min}}$  were required to match the location and steepness of the absorption trough. Larger X-ray column depths and lower radio-loudness fractions were introduced to obtain a large trough depth while staying below the limits imposed by the ARCADE-2 excess (see Fig. 11). These parameters are also listed along with all other models in Table 5

transition to  $\delta T_b \approx 0$  at the very end of the absorption feature, requires additional sources of ionizing photons (beyond what is provided by the obscured black holes and standard star formation scenarios). It is possible that these photons might be provided as black holes blow away their obscuring material, a process that we do not model in detail. However, an end to absorption feature consistent with EDGES and driven by ionization would contradict other probes. A more likely scenario might be enhanced heating from the same clearing. We have not attempted a systematic search

of parameter space and are hesitant to do so until the specific properties of the EDGES feature are verified. Thus, it is entirely possible that other EDGES-like models do exist without the short-comings of our two examples. We leave more systematic fitting of the EDGES signal to future studies.

We finally note that both of the scenarios that we have constructed to explain EDGES predict radio point-source populations that are above the detection threshold of upcoming surveys on the SKA1-MID (Fig. 14). It follows that these upcoming surveys have an important roll to play in validating or rejecting potential explanations of EDGES that involve discrete radio sources.

## 6 CONCLUSIONS

We have introduced a simple recipe for computing the impact of radio emission from black-hole seed growth on the 21 cm signal that can be incorporated into existing semi-numerical simulation frameworks that estimate emissivities from the halo collapse rate (e.g. *ares*, *21cmFAST*, and *simfast21*). We combined our modeling framework with the 21 cm global-signal formalism developed in Furlanetto (2006). For the first time, we compute the impact of radio emission from black holes self-consistently with the effects of their X-ray and UV emission. By studying the 21 cm global signal arising in a handful of illustrative scenarios, we have arrived at the following conclusions on the signatures of radio-loud black-holes during the Cosmic Dawn.

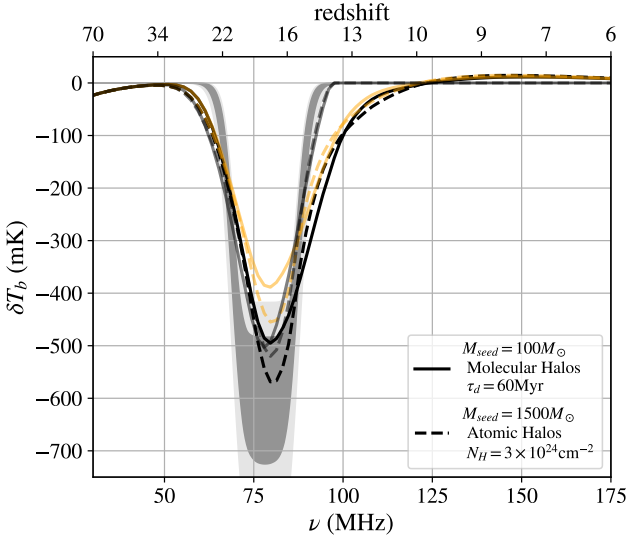


**Figure 10.**  $\delta T_b$  for two different EDGES-like models compared to the 68% and 95% contours of the detection in B18. We are able to produce the steep sides and large amplitude of the absorption trough through judicious choices of  $\tau_s$ ,  $T_{\text{vir}\star}^{\text{min}}$ , and  $\log_{10} N_{\text{HI}}$ . However, a  $\sim 100$  mK absorption feature remains out to  $z \approx 13$  unless significant HI ionization takes place by  $z \approx 13$ , inconsistent with recent Planck results (thin grey solid and dashed lines in this Figure and Fig. 12). Within our modeling framework, we are not able to produce a flat-bottom trough. The orange light lines denote models where the radio spectral index,  $\alpha_R$ , has been flattened from 1.1 to 0.5. Flatter spectral indices produce smaller absorption troughs as we found in Fig. 2.

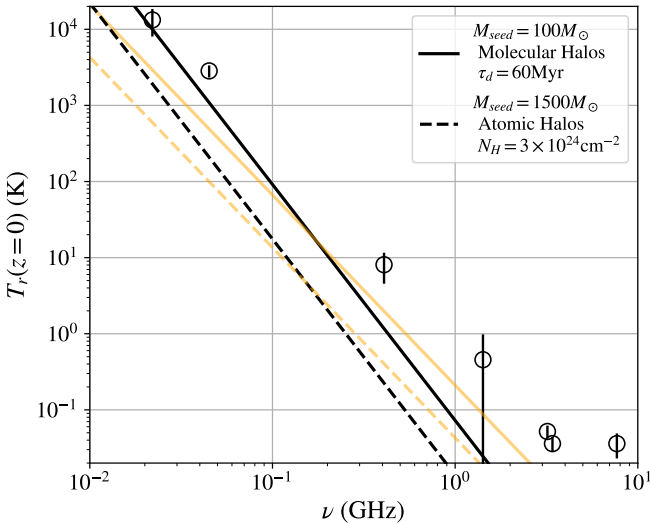


**Figure 11.** The same as Fig. 5 except now only comparing radio backgrounds from our EDGES-like models (Table 7) to other measurements of the excess radio monopole. Our EDGES-like models are below the level of excess.

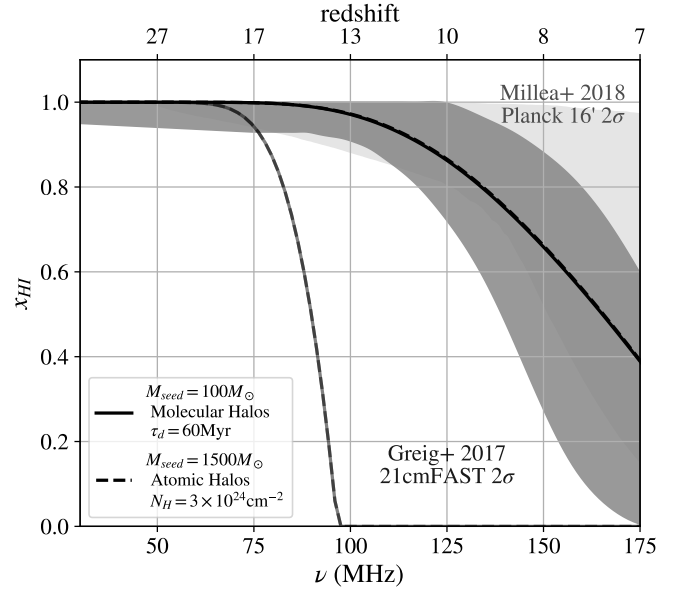


**Figure 12.** The same as Fig. 4 but now showing the two EDGES-like models summarized in Table 7. Light sets of lines (which reionize earlier) represent scenarios identical to those in Table 7 where the stellar ionizing escape fraction has been raised to  $f_{\text{esc}\star} = 1$  and  $N_\gamma = 10^4$  in order to make the absorption feature more consistent with the B18 detection (Fig. 10). While increased stellar reionization brings better agreement with the B18 detection, it violates complementary constraints on reionization.

(i) We find that if the first black-hole seeds were obscured column depths  $\gtrsim 10^{23} \text{ cm}^{-2}$ , radio-loudness levels similar to today will have a significant impact on the observed 21 cm global signal – at the level of tens to hundreds of percent. These significant effects are present even when the accretion rates are well below the Eddington limit. Thus, 21 cm experiments should be able to probe the radio-loudnesses of any rapidly growing black hole seeds that existed during and before the Cosmic Dawn absorption feature. This includes backgrounds from sub-nJy sources that are below the detection thresholds of any near term surveys. Hence, the global 21 cm signal may be the best way to constrain the existence of such sources. That said, sub-Eddington accretion rates do not produce a signature as dramatic as EDGES and further work is needed to determine how radio signatures are degenerate with other model parameters.

(ii) When duty cycles and Eddington ratios are close to unity, obscured radio-loud black holes can generate a Cosmic Dawn absorption feature that is significantly deeper and narrower than what is seen in models where star formation dominates. This is due to the fact that the co-moving black-hole emissivity in our model has the freedom to evolve faster than the star-formation rate density. The steepness of the sides of the absorption feature increase with decreasing Salpeter time and/or increased seed mass while the timing is primarily affected by seed and halo mass. The overall depth is controlled by X-ray luminosity, spectral hardness, and obscuration.

(iii) Radio-loud black holes are able to explain many aspects of the reported EDGES absorption feature including

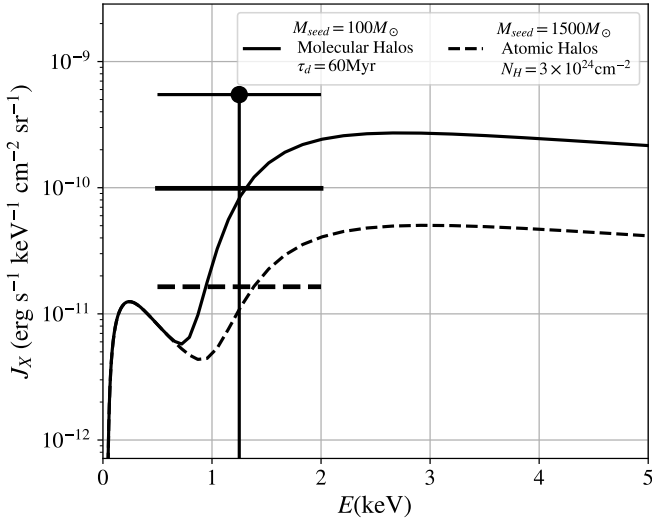


**Figure 13.** The same as Fig. 7 but now showing the X-ray background arising from the EDGES-like models in Table 7. The continuum arising from this model would exceed soft X-ray background limits.

its large depth, fast timing, and steep sides. Our model is also able to reproduce the radio-background excess observed by various experiments including ARCADE-2 and produces a soft X-ray backgrounds that is consistent with Chandra limits. While our model recreates the depth and steepness of the EDGES feature we were not able to produce a flat-bottomed absorption feature similar to what EDGES reports. In addition, our model cannot reproduce the rapid disappearance of absorption at the very end of the trough unless it is achieved through reionization of the Intergalactic medium at  $z \approx 14$ , either through stellar contributions or the black-holes themselves (by clearing obscuring material). Unfortunately, both scenarios are inconsistent with CMB and Ly  $\alpha$  forest constraints.

(iv) Current and upcoming point source surveys have an important roll to play in better constraining the models presented in this work. Firstly, the scenarios that we find are most consistent with EDGES also predict abundant populations of  $\sim 1 - 10 \mu\text{Jy}$  sources at 1.4 GHz. Secondly, seed/halo mass and accretion rate are all somewhat degenerate in our parameterization. These degeneracies might be removed through direct detection of these sources by surveys. Since models with less abundant but brighter and/or more massive seeds yield individual sources with higher flux. We find that the nominal SKA1-MID deep survey described in P15 will be capable of resolving a proposed model with  $1500 M_{\odot}$  seeds in atomic cooling halos (Figs. 8 and 9) which are accreting with a Salpeter time of 18 Myr while the ultra-deep survey can resolve sources in a scenario with  $100 M_{\odot}$  seeds in molecular cooling halos.

Our last point raises the exciting prospect that mid-band point source surveys and low frequency observations of redshifted 21 cm may be used in conjunction to unveil the so-far unknown radio properties of SMBH progenitors.

## ACKNOWLEDGEMENTS

We thank Michael Seiffert, Olivier Doré, Jordan Mirocha, Luis Mas-Ruibas and Phillippe Berger for helpful comments on this manuscript. AEW’s contribution was supported by an appointment to the NASA Postdoctoral Program at the California Institute of Technology Jet Propulsion Laboratory. Part of the research was carried out at the Jet Propulsion Laboratory, California Institute of Technology, under a contract with the National Aeronautics and Space Administration.

## CODE

All code used in this project is publicly available at [https://github.com/anguta/global\\_bh](https://github.com/anguta/global_bh). The authors acknowledge extensive use of the `colossus` library (Diemer 2017) which can be downloaded at <https://bdiemer.bitbucket.io/colossus/> along with the interpolation tables in `21cmFAST` (Mesinger et al. 2011) which is available at <https://github.com/andreimesinger/21cmFAST>. We also acknowledge use of the `numpy` (Oliphant 06), `scipy` (Jones et al. 01), and `matplotlib` (Hunter 2007) libraries.

## REFERENCES

- Alvarez M. A., Wise J. H., Abel T., 2009, *ApJ*, **701**, L133  
 Bañados E., et al., 2015, *ApJ*, **804**, 118  
 Bañados E., et al., 2018, *Nature*, **553**, 473  
 Barkana R., 2018, *Nature*, **555**, 71 EP  
 Barkana R., Loeb A., 2005, *ApJ*, **626**, 1  
 Barkana R., Outmezguine N. J., Redigolo D., Volansky T., 2018, preprint, [p. arXiv:1803.03091](https://arxiv.org/abs/1803.03091) ([arXiv:1803.03091](https://arxiv.org/abs/1803.03091))  
 Berlin A., Hooper D., Krnjaic G., McDermott S. D., 2018, preprint, [p. arXiv:1803.02804](https://arxiv.org/abs/1803.02804) ([arXiv:1803.02804](https://arxiv.org/abs/1803.02804))  
 Bird J., Martini P., Kaiser C., 2008, *ApJ*, **676**, 147  
 Bowman J. D., Rogers A. E. E., Monsalve R. A., Mozdzen T. J., Mahesh N., 2018, *Nature*, **555**, 67 EP  
 Cappelluti N., et al., 2013, *ApJ*, **769**, 68  
 Cirasuolo M., Celotti A., Magliocchetti M., Danese L., 2003, *MNRAS*, **346**, 447  
 Condon J. J., et al., 2012, *ApJ*, **758**, 23  
 Das A., Mesinger A., Pallottini A., Ferrara A., Wise J. H., 2017, *MNRAS*, **469**, 1166  
 Diemer B., 2017, preprint, ([arXiv:1712.04512](https://arxiv.org/abs/1712.04512))  
 Donoso E., Best P. N., Kauffmann G., 2009, *MNRAS*, **392**, 617  
 Dowell J., Taylor G. B., 2018, *ApJ*, **858**, L9  
 Ewall-Wice A., Chang T. C., Lazio J., Doré O., Seiffert M., Monsalve R. A., 2018, *ApJ*, **868**, 63  
 Feng C., Holder G., 2018, preprint, ([arXiv:1802.07432](https://arxiv.org/abs/1802.07432))  
 Fernandez E. R., Komatsu E., 2006, *ApJ*, **646**, 703  
 Fialkov A., Barkana R., 2019, arXiv e-prints, [p. arXiv:1902.02438](https://arxiv.org/abs/1902.02438)  
 Fialkov A., Barkana R., Visbal E., 2014, *Nature*, **506**, 197  
 Fialkov A., Cohen A., Barkana R., Silk J., 2017, *MNRAS*, **464**, 3498  
 Fialkov A., Barkana R., Cohen A., 2018, preprint, ([arXiv:1802.10577](https://arxiv.org/abs/1802.10577))  
 Field G. B., 1958, *Proceedings of the IRE*, **46**, 240  
 Fixsen D. J., et al., 2011, *ApJ*, **734**, 5  
 Fraser S., et al., 2018, preprint, [p. arXiv:1803.03245](https://arxiv.org/abs/1803.03245) ([arXiv:1803.03245](https://arxiv.org/abs/1803.03245))  
 Furlanetto S. R., 2006, *MNRAS*, **371**, 867  
 Furlanetto S. R., Stoever S. J., 2010, *MNRAS*, **404**, 1869



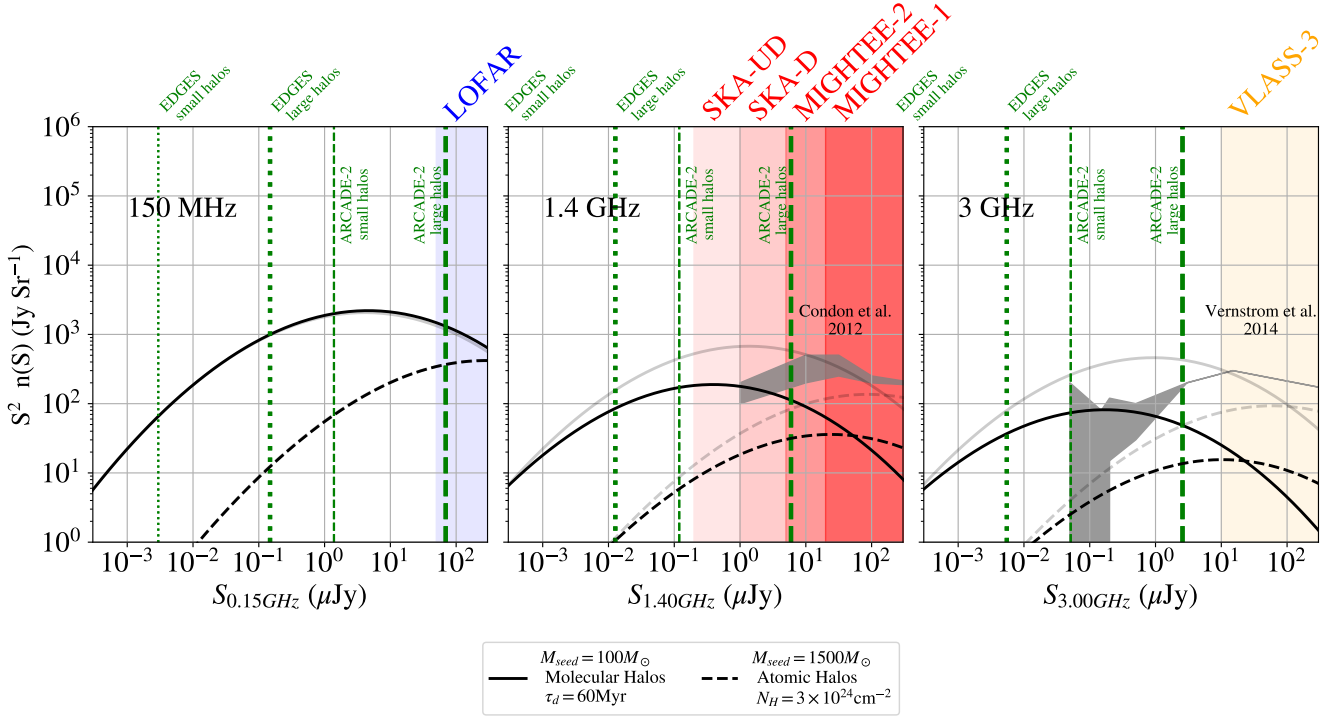


**Figure 14.** The same as Fig. 14 but now including the two EDGES-like models summarized in Table 7. Both models are consistent with the results of recent fluctuation analyses. The distribution peaks of both the Small and Large Halos models are resolved by the deep and ultra-deep SKA1-MID surveys. Thus, these surveys will be able to place interesting constraints on models of radio-loud black holes that might explain the EDGES feature. Light lines indicate models where the radio spectral index,  $\alpha_R$  has been flattened from 1.1 to 0.5. These flat spectral models are ruled out by existing fluctuation analyses.

Furlanetto S. R., Oh S. P., Briggs F. H., 2006, *Phys. Rep.*, **433**, 181

Ghisellini G., Sbarrato T., 2016, *MNRAS*, **461**, L21

Ghisellini G., Celotti A., Tavecchio F., Haardt F., Sbarrato T., 2014, *MNRAS*, **438**, 2694

Ghisellini G., Haardt F., Ciardi B., Sbarrato T., Gallo E., Tavecchio F., Celotti A., 2015, *MNRAS*, **452**, 3457

Greig B., Mesinger A., 2017, *MNRAS*, **465**, 4838

Haiman Z., Quataert E., Bower G. C., 2004, *ApJ*, **612**, 698

Heinz S., Sunyaev R. A., 2003, *MNRAS*, **343**, L59

Hills R., Kulkarni G., Meerburg P. D., Puchwein E., 2018, preprint, [p. arXiv:1805.01421](https://arxiv.org/abs/1805.01421) ([arXiv:1805.01421](https://arxiv.org/abs/1805.01421))

Hirano S., Hosokawa T., Yoshida N., Omukai K., Yorke H. W., 2015, *MNRAS*, **448**, 568

Hirata C. M., 2006, *MNRAS*, **367**, 259

Hunter J. D., 2007, *Computing In Science & Engineering*, **9**, 90

Ivezić Ž., et al., 2002, *AJ*, **124**, 2364

Ivezić Ž., et al., 2004, in *AGN Physics with the Sloan Digital Sky Survey*, Proceedings of a conference held in Princeton, NJ, USA, 27-31 July 2003, Edited by Gordon T. Richards and Patrick B. Hall, ASP Conference Series, Volume 311. San Francisco: Astronomical Society of the Pacific, 2004., p.347.

Jiang L., Fan X., Ivezić Ž., Richards G. T., Schneider D. P., Strauss M. A., Kelly B. C., 2007, *ApJ*, **656**, 680

Johnson J. L., Bromm V., 2007, *MNRAS*, **374**, 1557

Jones E., Oliphant T., Peterson P., et al., 2001–, SciPy: Open source scientific tools for Python, <http://www.scipy.org/>

Kaurov A. A., Venumadhav T., Dai L., Zaldarriaga M., 2018, preprint, [p. arXiv:1805.03254](https://arxiv.org/abs/1805.03254) ([arXiv:1805.03254](https://arxiv.org/abs/1805.03254))

Kellerman K. I., Sramek R., Schmidt M., Shaffer D. B., Green

R., 1989, *AJ*, **98**, 1195

Liu A., Pritchard J. R., Allison R., Parsons A. R., Seljak U., Sherwin B. D., 2016, *Phys. Rev. D*, **93**, 043013

Lusso E., et al., 2010, *A&A*, **512**, A34

Lusso E., Worsack G., Hennawi J. F., Prochaska J. X., Vignali C., Stern J., O’Meara J. M., 2015, *MNRAS*, **449**, 4204

Madau P., Haardt F., 2015, *ApJ*, **813**, L8

Madau P., Rees M. J., Volonteri M., Haardt F., Oh S. P., 2004, *ApJ*, **604**, 484

Marchese E., Della Ceca R., Caccianiga A., Severgnini P., Corral A., Fanali R., 2012, *A&A*, **539**

McGreer I. D., Helfand D. J., White R. L., 2009, *AJ*, **138**, 1925

McQuinn M., 2016, *Annual Review of Astronomy and Astrophysics*, **54**, 313

Mebane R. H., Mirocha J., Furlanetto S. R., 2017, preprint, [p. arXiv:1710.02528](https://arxiv.org/abs/1710.02528) ([arXiv:1710.02528](https://arxiv.org/abs/1710.02528))

Merritt D., Ferrarese L., 2001, *MNRAS*, **320**, L30

Mesinger A., Furlanetto S., Cen R., 2011, *MNRAS*, **411**, 955

Mesinger A., Ferrara A., Spiegel D. S., 2013, *MNRAS*, **431**, 621

Millea M., Bouchet F., 2018, preprint, [p. arXiv:1804.08476](https://arxiv.org/abs/1804.08476) ([arXiv:1804.08476](https://arxiv.org/abs/1804.08476))

Mineo S., Gilfanov M., Sunyaev R., 2012, *MNRAS*, **419**, 2095

Mirabel I. F., Dijkstra M., Laurent P., Loeb A., Pritchard J. R., 2011, *A&A*, **528**, A149

Mirocha J., Furlanetto S. R., 2018, preprint, [p. arXiv:1803.03272](https://arxiv.org/abs/1803.03272) ([arXiv:1803.03272](https://arxiv.org/abs/1803.03272))

Morales M. F., Wyithe J. S. B., 2010, *ARA&A*, **48**, 127

Mortlock D. J., et al., 2011, *Nature*, **474**, 616

Muñoz J. B., Loeb A., 2018, preprint, ([arXiv:1802.10094](https://arxiv.org/abs/1802.10094))

Nandra K., Pounds K. A., 1994, *MNRAS*, **268**, 405

Oh S. P., 2001, *ApJ*, **553**, 499

- Oliphant T., 2006–, NumPy: A guide to NumPy, USA: Trelgol Publishing, <http://www.numpy.org/>
- Pacucci F., Mesinger A., Mineo S., Ferrara A., 2014, *MNRAS*, **443**, 678
- Pacucci F., Ferrara A., Volonteri M., Dubus G., 2015, *MNRAS*, **454**, 3771
- Planck Collaboration et al., 2016, *A&A*, **596**, A107
- Pospelov M., Pradler J., Ruderman J. T., Urbano A., 2018, *Phys. Rev. Lett.*, **121**, 031103
- Prandoni I., Seymour N., 2015, in *Advancing Astrophysics with the Square Kilometre Array (AASKA14)*. p. 67 ([arXiv:1412.6512](https://arxiv.org/abs/1412.6512))
- Pritchard J. R., Loeb A., 2012, *Reports on Progress in Physics*, **75**, 086901
- Ripamonti E., Mapelli M., Zaroubi S., 2008, *MNRAS*, **387**, 158
- Santos M. G., Amblard A., Pritchard J., Trac H., Cen R., Cooray A., 2008, *ApJ*, **689**, 1
- Saxena A., Röttgering H. J. A., Rigby E. E., 2017, *MNRAS*, **469**, 4083
- Seiffert M., et al., 2011, *ApJ*, **734**, 6
- Shabala S. S., Ash S., Alexander P., Riley J. M., 2008, *MNRAS*, **388**, 625
- Shankar F., Crocce M., Miralda-Escudé J., Fosalba P., Weinberg D. H., 2010, *ApJ*, **718**, 231
- Shankar F., Weinberg D. H., Miralda-Escudé J., 2013, *MNRAS*, **428**, 421
- Sharma P., 2018, preprint, ([arXiv:1804.05843](https://arxiv.org/abs/1804.05843))
- Sheth R. K., Tormen G., 1999, *MNRAS*, **308**, 119
- Shimwell T. W., et al., 2017, *A&A*, **598**, A104
- Singal J., Petrosian V., Lawrence A., Stawarz L., 2011, *ApJ*, **743**
- Singal J., et al., 2018, *Publications of the Astronomical Society of the Pacific*, **130**, 036001
- Smith B., Regan J., Downes T., Norman M., O’Shea B., Wise J., 2018, preprint, p. [arXiv:1804.06477](https://arxiv.org/abs/1804.06477) ([arXiv:1804.06477](https://arxiv.org/abs/1804.06477))
- Tanaka T. L., O’Leary R. M., Perna R., 2016, *MNRAS*, **455**, 2619
- Titarchuk L., 1994, *ApJ*, **434**, 570
- Turner R. J., Shabala S. S., 2015, *ApJ*, **806**, 59
- Venumadhav T., Dai L., Kaurov A., Zaldarriaga M., 2018, preprint, p. [arXiv:1804.02406](https://arxiv.org/abs/1804.02406) ([arXiv:1804.02406](https://arxiv.org/abs/1804.02406))
- Vernstrom T., et al., 2014, *MNRAS*, **440**, 2791
- Volonteri M., Haardt F., Ghisellini G., Della Ceca R., 2011, *MNRAS*, **416**, 216
- Willott C. J., et al., 2010, *AJ*, **140**, 546
- Wu X.-B., et al., 2015, *Nature*, **518**, 512
- Yue B., Ferrara A., Salvaterra R., Xu Y., Chen X., 2013, *MNRAS*, **433**, 1556
- Zaroubi S., Thomas R. M., Sugiyama N., Silk J., 2007, *MNRAS*, **375**, 1269

This paper has been typeset from a  $\text{\TeX}/\text{\LaTeX}$  file prepared by the author.